3-22-2012

Automatic Target Recognition for Hyperspectral Imagery

Kelly D. Friesen

AUTOMATIC TARGET RECOGNITION FOR HYPERSPECTRAL IMAGERY

THESIS

Kelly D. Friesen, Captain, USAF

AFIT-OR-MS-ENS-12-11

DEPARTMENT OF THE AIR FORCE
AIR UNIVERSITY

AIR FORCE INSTITUTE OF TECHNOLOGY

Wright-Patterson Air Force Base, Ohio

The views expressed in this thesis are those of the author and do not reflect the official policy or position of the United States Air Force, Department of Defense, or the United States Government.

AFIT-OR-MS-ENS-12-11

AUTOMATRIC TARGET RECOGNITION FOR HYPERSPECTRAL IMAGERY

THESIS

Presented to the Faculty

Department of Operational Sciences

Graduate School of Engineering and Management

Air Force Institute of Technology

Air University

Air Education and Training Command

In Partial Fulfillment of the Requirements for the

Degree of Master of Science in Logistics Management

Kelly D. Friesen, BA

Captain, USAF

March 2012

AFIT-OR-MS-ENS-12-11

AUTOMATRIC TARGET RECOGNITION FOR HYPERSPECTRAL IMAGERY

Kelly D. Friesen, BA
Captain, USAF

Approved:

// Signed //	24 March 2012
Dr. Kenneth W. Bauer (Chairman)	date
// Signed //	24 March 2012
Mark A. Friend, Lt Col, USAF (Member)	date

Abstract

Automatic target detection and recognition in hyperspectral imagery offer passive means to detect and identify anomalies based on their material composition. In many combat identification approaches through pattern recognition, a minimum level of confidence is expected with costs associated with labeling anomalies as targets, non-targets or out-of-library. This research approaches the problem by developing a baseline, autonomous four-step automatic target recognition (ATR) process: 1) anomaly detection, 2) spectral matching, 3) out-of-library decision, and 4) non-declaration decision. Atmospheric compensation techniques are employed in the initial steps to compare truth library signatures and sensor processed signatures. ATR performance is assessed and additionally contrasted to two modified ATRs to study the effects of including steps three and four. Also explored is the impact on the ATR with two different anomaly detection methods.

To my father and mother

Acknowledgements

First and foremost I would like to thank my Lord and Savior Jesus Christ for the strength and wisdom to accomplish this Master's Degree program.

Next, I'd like to thank my thesis advisor, Dr. Kenneth Bauer. His guidance and direction helped keep me focused throughout the process while his mentorship provided clarity when determining what the results truly meant. His direct, calm approach to getting a quality product without adding unnecessary stress was a key to my success, and it is a lesson I will take with me as I continue to progress in my career. I would also like to thank my thesis reader, Lt Col Mark Friend, for your support and encouragement along the way.

Thank you to Mr. Trevor Bihl for all the time spent teaching me concepts of HSI basics, atmospheric compensation, radiative transfer, and for answering all my MATLAB questions. Thank you also to Ms. Kelly Bush, Capt Jason Williams, and fellow classmates for your added assistance.

Finally, I would like to thank my family. To my wife, I love you and can't thank you enough for your love and support throughout our time here. You provided a home that I wanted to return to after long hours of studying and are raising a wonderful little girl. To my daughter, thank you for bringing a smile to face every day I came home. I love to see how much you have grown each day; you've gone from a little baby just learning to take her first steps to a wild, talkative, big girl. Lastly, to my unborn daughter, I can't wait to meet you in a few months!

Kelly D. Friesen

Table of Contents

Page

List of Figures

Page

List of Tables

Page

AUTOMATIC TARGET RECOGNITION WITH
HYPERSPECTRAL IMAGES

I. Introduction

Background

"More with less" is a common phrase heard through the halls of many Air Force (AF) organizations, their sister-services and other Department of Defense organizations. Ironically, the amount of information, including remotely sensed data, provided to the warfighter has increased dramatically. In a recent email, LtGen David Goldfein, AF Central Command Commander and Combined Forces Air Component Commander, stated that since 2003 remotely piloted aircraft crews have provided persistent ISR processing over 50,000 images (Goldfein, 2012). Of those images hyperspectral imaging is sure to be included.

Hyperspectral images consist of large amounts of spectral and spatial data and have been used in numerous applications to include terrain classification, environmental monitoring, agricultural monitoring, geological exploration, and surveillance (Stein, Beaven, Hoff, Winter, Schaum, & Stocker, 2002). With decreases in manning levels and the ever increasing data load, more efficient algorithms are required to process data.

Problem Statement

Automatic target recognition's (ATR) goal is to identify an unknown object, or target, from a known signature (Paul A. S., Shaw, Das, & Mitra, 2003). From the literature it was found that ATR processes for hyperspectral imagery (HSI) consist primarily of two steps: anomaly detection and classification. While there may be other steps included in the algorithm, the essence is anomaly detection and classification, i.e., Chang and Chiang outline a three-stage process which includes anomaly detection, clustering of anomalies, and classification (Chang & Chiang, 2002). This thesis

investigates a four-step ATR process which consists of the common anomaly detection and classification steps and is followed by an out-of-library (OOL) decision step and finally a non-declaration (NDEC) decision step. The final two steps are added to assess if there is any performance improvement to the ATR process.

Methodology

The methodology the ATR consists of is the aforementioned four steps and a step zero. The steps are broken down as follows:

Step 0: Loading HSI data and library reference signals

Step 1a: Region of Interest Generator (anomaly detection)

Step 1b: Atmospheric Compensation Estimation

Step 2: Matched Filtering for initial classification

Step 3: OOL decisions

Step 4: NDEC decision for final classification

The measures of performance for the ATR are the commonly used true positive fractions and false positive fractions, which form a receiver operating characteristic (ROC) curve.

Research Objectives

The focus of this effort is to develop a baseline, autonomous four-step ATR process for HSI and to assess the performance. A comparative ATR assessment given two different region of interest generators will also be provided. Finally, an assessment of how the incremental inclusion of the OOL step and NDEC step affect ATR performance is given.

Overview

This thesis contains five chapters: an introduction, a literature review, methodology, results, and a discussion. The introduction provides a brief overview of the thesis. The literature review lays the ground work of previous HSI research to include HSI basics, radiative transfer and atmospheric compensation, anomaly detection, classification, OOL decision techniques, and NDEC decision methods. The methodology walks through the process to obtain the baseline, four-step ATR process. The results provide answers to the research objectives. The last chapter provides the contributions of the thesis to ATR for HSI along with ideas for future research.

II. Literature Review

This chapter describes significant contributions applicable to developing an ATR process for HSI. Relevant literature is outlined and described in the following 11 sections: HSI Basics, Hyperspectral Digital Imagery Collection Experiment (HYDICE), Radiative Transfer, Image Collection, Reference Library Creation, Atmospheric Compensation, Anomaly Detection, Region of Interest Generator, Classification, Out-of-Library Decision, and Non-Declaration Decision.

Hyperspectral Basics

All objects reflect, emit, and absorb electromagnetic (EM) energy; the degree at which these things take place is dependent upon the object's material composition. The most familiar component of the EM spectrum consists of the wavelengths 0.4 – 0.7 μm, the visible region (V). Figure 1 shows this portion of the EM spectrum as well as the entire spectrum. Typical EM spectrum areas of interest, in remote sensing, include the visible to near-infrared (VNIR) region between 0.4 and 1.1 μm, the shortwave infrared (SWIR) region between 1.1 and 3 μm, midwave-infrared (MWIR) from 3 – 5 μm, and the longwave-infrared (LWIR) spectrum from 5 – 14 μm.

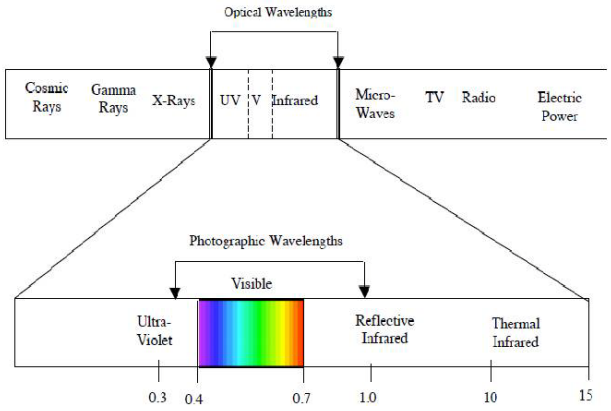

Figure 1. Electromagnetic Spectrum, taken directly from (Landgrebe, 2003)

An example of a system that works in the visible region would be a digital camera; which captures information corresponding to reflected light in the red, green, and blue wavelength bands. For a single image, specifically for each pixel of the image, the information collected consists of the amount of energy reflected, in each discrete, noncontiguous band. When the information from the three bands is overlaid upon each other an image takes the form of what we are used to seeing.

A digital camera can be considered a simple multispectral imaging system. A multispectral imaging system typically operates in three to 20 different EM bands. Typically, multispectral sensors (such as those on LandSAT) collect visible and NIR bands (Connor & Mooneyhan, 1985). There is unfortunately no rule-of-thumb for the number of bands that defines a multispectral image; the number of bands is not necessarily important, the primary definition of a multispectral imaging system is having discontinuous bands with large spectral bandwidths (Eismann, 2011). Spectral bandwidths can be defined for our purposes as the spectral sample period between collected wavelengths; for multispectral systems this is on the order of 100nm (Connor & Mooneyhan, 1985). A large spectral bandwidth such as this provides a low spectral resolution and is not suitable for detecting fine spectral features (Connor & Mooneyhan, 1985) (Eismann, 2011).

A hyperspectral image is essentially a continuous spectral and spatial image collected over a large portion of the EM spectrum. Instead of operating in three spectral bands in the visible region or multiple distinct bands covering multiple parts of the EM spectrum, HSI spans a large contiguous portion of the EM spectrum (Eismann, 2011). HSI offers finer spectral resolution, with a spectral bandwidth typically on the order of 10nm (Lillisand & Kiefer, 2000) (Manolakis & Shaw, 2002) (Eismann, 2011). Spectral resolution is limited by a number of factors including characteristics of the focal plane array, optical system parameters, etc (Eismann, 2011). It is the capability to capture

image data in this fashion that also distinguishes multispectral and hyperspectral images. The combination of HSI covering a large portion of the EM spectrum and fine spectral resolution means HSI data typically has a larger number of spectral bands when compared to multispectral sensors due to its physical properties (Eismann, 2011). In many applications, e.g. HYDICE (defined in the next section), HSI operates in over 200 contiguous bands.

Hyperspectral remote sensing can be conceptualized as a combination of two sensing modes: panchromatic and spectroscopy (Eismann, Stocker, & Nasrabadi, 2009) (Eismann, 2011). Panchromatic imaging captures spatial radiance information about a scene in one wavelength band to create a black and white image (Eismann, 2011). Typically this occurs over the visible band. Spectrometers measure the variation of light from a one dimensional source across multiple wavelengths, enabling detection of molecular composition (Eismann, 2011). In essence hyperspectral sensors can be considered as multiple one dimensional spectrometers arranged to capture spatial and spectral information; each spatial pixel therefore captures the entire spectral profile of a given location.

There are three primary purposes for HSI remote sensing, anomaly detection, change detection and spectral signature matching (Smetek & Bauer, 2008). Of interest herein are anomaly detection and spectral signature matching. Fundamentally we are interested in extracting information that can be used to detect anomalies that are statistically different from the background and identifying them through reference library signatures (Eismann, 2011).

Hyperspectral Digital Imagery Collection Experiment

The imagery data set used for this study is from the HYDICE imaging spectrometer, specifically images taken from the Forest Radiance I and Desert Radiance

II datasets. Used for the advancement of defense applications for hyperspectral remote sensing in VNIR/SWIR, HYDICE provides spectral imaging over 400 – 2500 nm from a fixed wing aircraft platform, using pushbroom collection (Rickard, Basedow, Zalewski, & Silverglate, 1993) (Eismann, 2011). The sensor generates swath widths of 320 pixels wide with 210 bandwidths per pixel (Eismann, 2011). A pictorial representation of the pushbroom technique is in Figure 2.

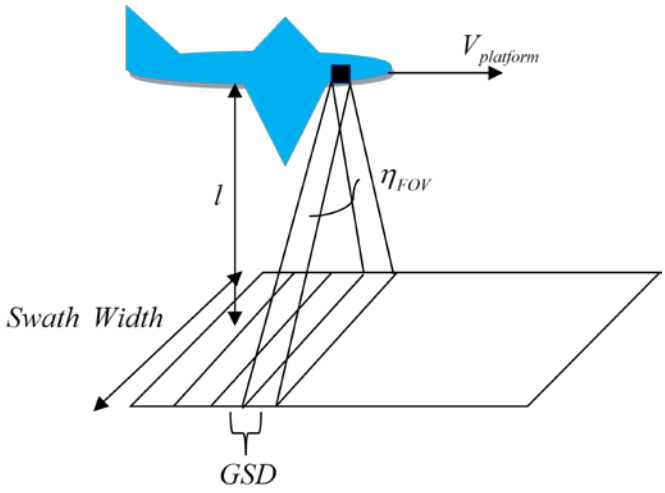

Figure 2. Pushbroom scanning technique (Bihl, unpublished)

Radiative Transfer

The energy received by an HSI sensor is called radiance energy; a unit of power per unit area per solid angle (Eismann, 2011). Because light which reaches a sensor passes through the atmosphere and reflects off of objects (termed scattering), data reaching a sensor is not spectrally pure (Eismann, 2011). The process in which this occurs is termed "radiative transfer" (Eismann, 2011). Depending on the reference and descriptions, radiative transfer quantities are divided into either three (Smetek, 2007), four (Kerekes, 1998) or five (Eismann, 2011) segments and describe the radiative transfer of spectral radiance reaching a sensor. This is not to say that there is dispute about what factors are

present, merely how they are combined. These can be generally described as (Eismann, 2011), (Smetek, 2007), and (Kerekes, 1998):

1. Directly reflected radiance off the target of interest to the sensor (Eismann, 2011) (Kerekes, 1998) (Smetek, 2007);
2. Diffuse or indirect solar radiance first scattered by the atmosphere then reflected off the target into the sensor (Eismann, 2011) (Kerekes, 1998);
3. Scattered radiance which first scatters off of an adjacent object on the ground, then reflects off the target into the sensor (Eismann, 2011);
4. Background radiance from adjacent objects on the ground reflected into the sensor (Eismann, 2011) (Kerekes, 1998) and;
5. Upwelling or path radiance is radiance scattered by the atmosphere directly to the sensor without reaching an object (Eismann, 2011) (Smetek, 2007) (Kerekes, 1998).

Smetek (Smetek, 2007) combined these terms into three categories corresponding to Eismann (Eismann, 2011) and Healey and Slater's (Healey & Slater, 1999) grouping of the first type as *direct solar irradiance*, the second through fourth will be called *indirect downwelling radiance*, and the fifth being *upwelling path radiance*. The general radiative transfer model is visually depicted in Figure 3.

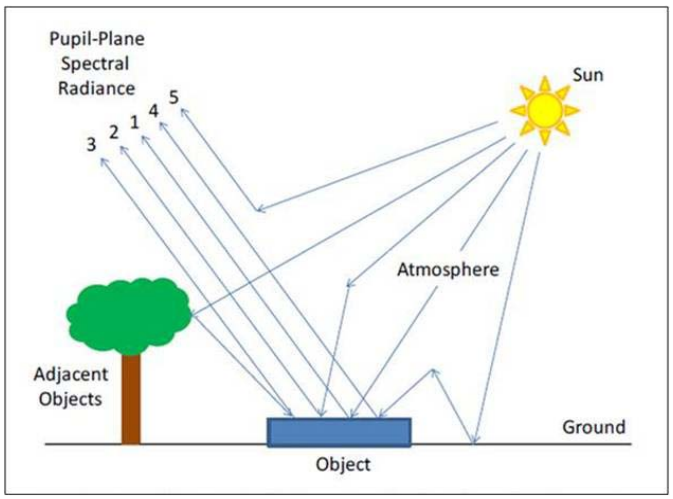

Figure 3. Radiative transfer process for the reflective case, taken directly from (Eismann, 2011)

Image Collection

Once reaching the sensor, radiance data passes through the optics of the HSI system being focused on the focal plane array (Eismann, 2011). The focal plane array contains detectors which converts collected light into an electrical signal (Eismann, 2011). The collected electrical signal is gathered by system electronics and manipulated into a data object known as an "image cube" or "hyper cube." The first two dimensions of the image cube account for the spatial dimensionality. They are referenced by *m* number of rows and *n* number of columns. The third dimension, *p*, of the image cube refers to the span of spectral bands collected by the HSI sensor.

For analysis, it is computationally simpler to manipulate two-dimensional matrices versus three or more dimensions. Therefore, the image cube data is mapped to a two-dimensional data matrix, *X*, such that each element corresponds to the signature reading for a single image pixel location with a different band. For example, for the element x_{mnp} in the data matrix in Figure 4, *p* is the band for the pixel located in row *m*, column *n*. Once the data matrix has been generated standard multivariate analysis

techniques can be used to analyze the data. Such techniques could include principal component analysis (PCA), discriminant analysis, and cluster analysis.

Each row of X is commonly referred to as a pixel vector. These pixel vectors can then be plotted against the collected spectral bands to create a spectral signature for each of $m \times n$ pixel locations. For example, in Figure 4 the three lines of the Spectral Signatures plot could represent the signatures of three different materials (Smetek & Bauer, 2008). The entire process is depicted in Figure 4.

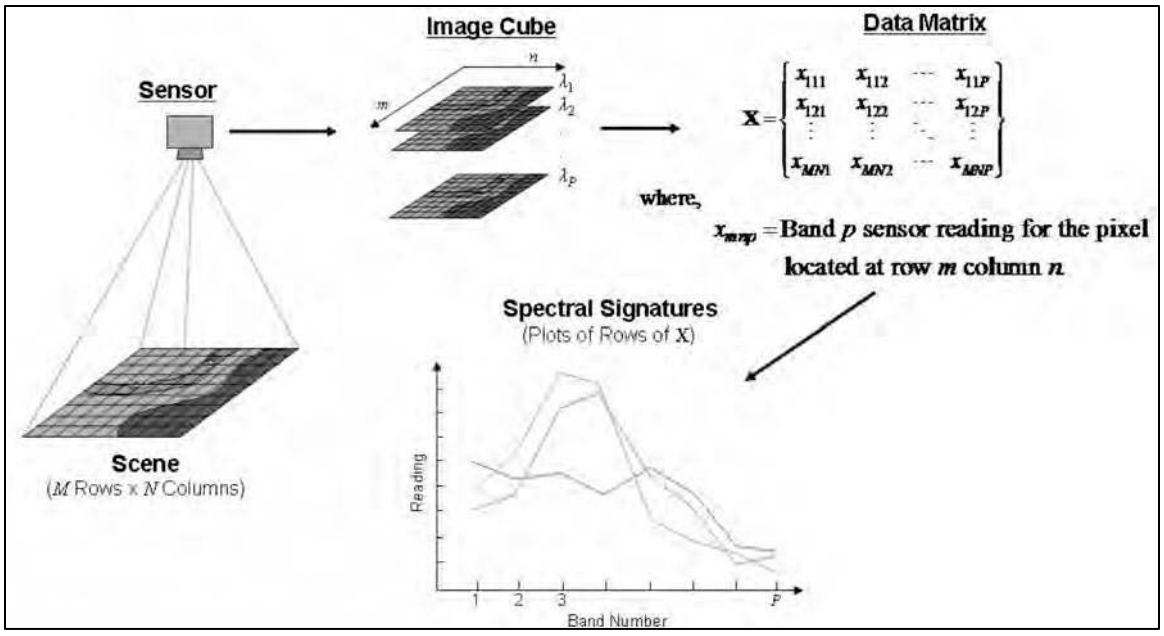

Figure 4. The basic hyperspectral imaging process and data representation, taken directly from (Smetek & Bauer, 2008)

Reference Library Creation

Most reference signature libraries are collected in controlled laboratory environments using spectrometers or semi-controlled environments on the ground using portable field spectrometers. This poses a challenge for comparisons with collected images, since the spectral signatures do not contain atmospheric effects; they contain

only what is known as reflectance. Reflectance signatures are those signals that would be recorded by a spectrometer held at close proximity to the material of interest (SpecTIR: Imagery with Substance). Therefore, for spectral signature comparison converting reflectance to radiance by estimating the atmospheric effects in an image must take place.

Atmospheric Compensation

The presence of unknown parameters such as illumination and atmospheric conditions are present in all images and need to be addressed to accomplish the goal of extracting a material's spectral properties (Eismann, 2011). Atmospheric compensation is performed to convert radiance energy to reflectance, or vice versa, with limited knowledge of illumination and atmospheric conditions. There are two categories for atmospheric compensation: in-scene methods and model-based methods. For this research we will be concerned with applying in-scene methods due to the ability to automate this process.

In-Scene Methods

Of the two categories the in-scene method is easier to intuitively understand and less computationally complex. In-scene methods require some *a priori* spectral information concerning the expected materials within the image. This information serves to guide the estimation of the atmospheric conditions. Two primary methods will be considered: the empirical line method and vegetation normalization. Both methods use in-scene ground objects and corresponding known reference reflectance data to compute atmospheric absorption properties (Eismann, 2011). The goal of both methods is to create a gain, $\hat{a}(\lambda)$, and offset, $\hat{b}(\lambda)$, for use in a linear approximate,

$$Rad(\lambda) = \hat{a}(\lambda) \cdot Refl(\lambda) + \hat{b}(\lambda) \quad (1)$$

which can be applied to a reflectance library to convert library reflectance to radiance units. The gain and offset are respectively calculated by

$$\hat{a}(\lambda) = \frac{L_2(\lambda) - L_1(\lambda)}{\rho_2(\lambda) - \rho_1(\lambda)} \tag{2}$$

and

$$\hat{b}(\lambda) = \frac{L_1(\lambda)\rho_2(\lambda) - L_2(\lambda)\rho_1(\lambda)}{\rho_2(\lambda) - \rho_1(\lambda)} \tag{3}$$

where ρ_i are known reflectance signatures and L_i are corresponding radiance measurements. The gain and offset equation elements are formed in one of two ways. First, is the empirical line method (ELM) and second, vegetation normalization (VN), which requires in-scene detected vegetation to serve as a known quantity.

Empirical Line Method

ELM is directly related to Equation (1) and used for reflectance estimation in the VNIR/SWIR spectral regions. This method requires at least two image pixels with known reflectance signatures, ρ_i, and corresponding radiance measurements, L_i, to obtain a gain and offset estimation. This technique can be further applied when more than two known reflectance signatures are available using linear least-squares regression analysis. Unfortunately, in regards to a fully automated process, having known reflectance signatures becomes its primary limitation (Eismann, 2011). Because of this limitation this study will focus on the use of VN to arrive at the gain and offset values.

Vegetation Normalization

To locate vegetation within an image normalized-difference vegetation index (NDVI) is applied. NDVI was first introduced by Rouse *et al.* while monitoring

vegetation conditions to assess the effects on regional growth conditions (Rouse, Hass, Schell, & Deering, 1973). A high NDVI score is an indication of healthy vegetation (Eismann, 2011). For example Figure 5 (a) shows the true red, green, blue (RGB) spectral representation of the HYDICE image ARES3F and Figure 5 (b) is the ARES3F image based on NDVI scores. Here we see that the vegetation areas have higher overall NDVI scores than the dirt patch in the middle of the image and the road ways on the right-hand side of the image.

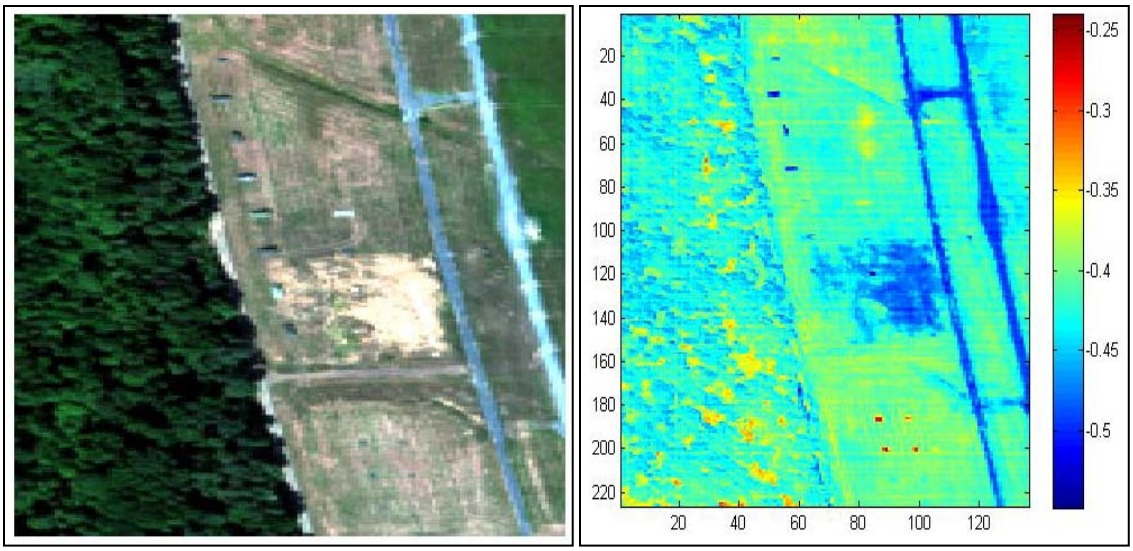

(a) (b)

Figure 5. HYDICE image ARES3F a) RGB representation, b) NDVI representation

Vegetation normalization builds upon ELM. Instead of manually locating image pixel(s) of known reflectance signatures, vegetation normalization uses vegetation as one of the reference signatures. This is accomplished under the assumption that vegetation reflectance signatures have a distinct shape and most images will contain a fair amount of vegetation. To identify the vegetation the NDVI equation,

$$NDVI = \frac{L_p(860\ nm) - L_p(660\ nm)}{L_p(860\ nm) + L_p(660\ nm)} \quad (4)$$

is applied (Eismann, 2011). L_p(860 nm) and L_p(660 nm) refer to the sensor readings (signatures) of a pixel in the NIR and red light bands, respectively. Next, only high NDVI values are considered based on a given threshold, relative to each image; this vector is then averaged to represent the radiance measurement for vegetation in the image (Eismann, 2011). This is the first radiance signature used to calculate the gain and offset.

The second radiance signature is determined by simply creating a shade spectrum such that the minimum image radiance value is used for each frequency band (Eismann, 2011). The first known reflectance signature applied is a known vegetation signature available from a truth library. The second is simply a vector of zeros of similar dimensions as the vegetation signature. With the four signatures established ELM Equations (2) and (3) can now be used to calculate the gain and offset.

Limitations of NDVI include the fact that NDVI will capture pixels that include "partially illuminated and shadowed vegetation spectra" as well as "fully illuminated vegetation spectra". Therefore, these pixels will not accurately match reference vegetation spectrum. Another limitation deals with the consistency of the spectral characteristics of healthy vegetation. Ideally, the spectral characteristics could be represented by a single reflectance spectrum; however, this is not the case. Figure 6 shows the variability of a few different types of vegetation (Eismann, 2011).

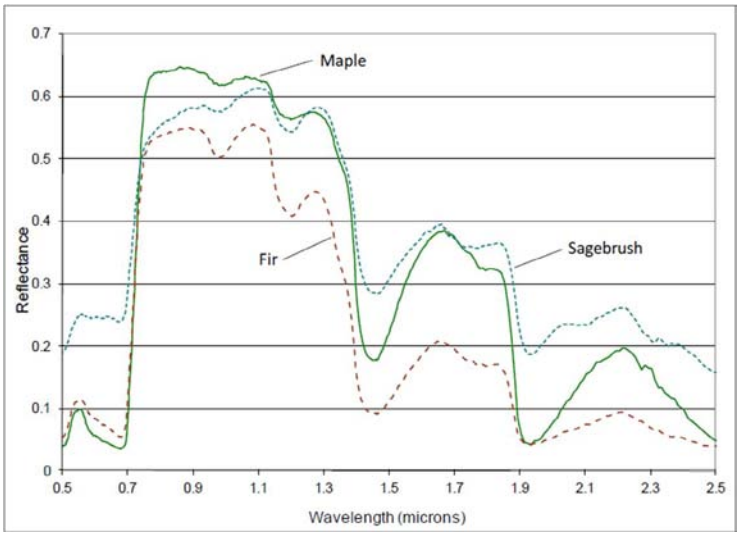

Figure 6. Vegetation Reflectance Spectra, taken directly from (Eismann, 2011)

Qinjiu and Xiangjun note that since the concept of vegetation indices were introduced more than 40 have been designed (Qinjiu & Xiangjun, 1998) (Du, Zhang, Yuan, Liu, & Zhang, 2007). Additional vegetation indices were created to account for other situations include the Bare Soil Index (Chen *et al.*, 2004), Soil Adjusted Vegetation Index (SAVI) (Huete, 1988), and Transformed Difference Vegetation Index (TDVI) (Bannari, Asalhi, & Teillet, 2002).

Model-Based Methods

Model-based methods can be quite accurate in regards to capturing atmospheric conditions such as illumination, transmission, and path radiance. They use a radiative transfer model, such as MODTRAN, as the basis for atmospheric compensation, which estimates various atmospheric conditions at the time an image was acquired (Smetek, 2007). While the atmospheric conditions are numerically computed, there are a number of atmospheric conditions that must be precisely specified, which are typically unknown (Ientilucci & Bajorski, 2006). The benefit of the model-based methods is the spectral variation of the unknown atmospheric conditions is constrained, thus making estimation

of these conditions easier to deal with in some scenarios (Eismann, 2011). However, estimating these unknown conditions can be time consuming (Ientilucci & Bajorski, 2006), requires specific knowledge of the scene conditions, and does not allow for automation to be completed in a timely manner, a goal of this study.

Anomaly Detection

Detection is formally defined as the act of discovering or noticing the presence of something hidden or hard to see (Merriam-Webster). In the case of anomaly detection, the "something hidden or hard to see" is a target of interest, in other words a statistical anomaly when compared to the background. The anomaly can be classified one of two ways; either a target is present or is not present (Shaw & Manolakis, 2002).

There are two types of target detection algorithms for HSI: spectral anomaly detection algorithms and spectral matching detection algorithms (Manolakis, Lockwood, Cooley, & Jacobson, 2009). Anomaly detection of course is categorized as the former. An anomaly is detected when an image pixel(s) is spectrally different from the remaining pixels in the image; those remaining pixels are also called background pixels. If there is no *a priori* information regarding the anomaly signatures the background is modeled. The potential anomaly signature is compared to the background signature and if it is not well-described by the background model, an anomaly is declared (Madar, Kuybeda, Malah, & Barzohar, 2009) (Chang & Chiang, 2002). While there are a number of different background models or anomaly detectors there are two basic categories: the local anomaly detector and the global anomaly detector (Rosario, 2006).

Local Anomaly Detector

The local anomaly detector uses processing windows to characterize the background pixels in the form of pixel vectors. The center pixel vector is compared to the remaining pixel vectors in the window to determine if an anomaly is present. The

window moves to the next pixel and an anomaly determination is made again. This process continues until each pixel in the HSI image has been characterized as background or anomaly (Smetek, 2007).

The primary advantage of the local anomaly detector is a high rate of anomaly detection. This is due to a high number of degrees of freedom allowing for the background model to be tightly fitted to the background data. However, this can also be a disadvantage because over-fitting can occur, causing a high false-alarm rate (Madar *et al.*, 2009). Over-fitting occurs when the model (or detector) too acurately models the training data and essentially causes no variation in the window pixels (Ratner). False-alarm rates can also increase due to isolated spectral anomalies. For example, a grass plain region with a few trees will detect the trees as anomalies even if the trees exist in another region (Stein, Beaven, Hoff, Winter, Schaum, & Stocker, 2002). "Generally, this [high false-alarm rate] happens due to the well known phenomenon that the number of training data pixels has to be significantly higher than the number of the model degrees of freedom. Since the number of free parameters in local background models is proportional to the data size, the model over-fitting problem is almost inevitable." (Madar *et al.*, 2009)

Another disadvantage of the local anomaly detector is the decreased ability to detect large, multiple-pixel anomalies. In order to detect such anomalies a large processing window is needed so that the anomalies do not dominate the window statistics. But if the window is too large the clutter may be too sufficient to detect an anomaly (Smetek, 2007). The Reed-Xiaoli detector is one of the most common local anomaly detection algorithms.

Reed-Xiaoli Detector

The Reed-Xiaoli (RX) detector was first introduced by Irving S. Reed and Xiaoli Yu in 1990 (Reed & Yu, 1990). It has since served as the anomaly detection standard. Originally adapted for multispectral sensors it was proven that it was a viable means for

HSI too. Summarized by Stein *el al.* (Stein *et al*., 2002) and then later by Eismann (Eismann, 2011) and Smetek (Smetek, 2007), the RX detector was derived using a generalized likelihood ratio test (GLRT). Of importance, when it is assumed that the processing window pixel vectors are normally distributed with mean $\boldsymbol{\mu}$ and covariance S Reed and Yu show that the GLRT reduced to:

$$RX(\boldsymbol{x}) = (\boldsymbol{x} - \widehat{\boldsymbol{\mu}})^T \left(\frac{N}{N+1} S + \frac{N}{N+1} (\boldsymbol{x} - \widehat{\boldsymbol{\mu}})(\boldsymbol{x} - \widehat{\boldsymbol{\mu}})^T \right)^{-1} (\boldsymbol{x} - \widehat{\boldsymbol{\mu}}) \tag{5}$$

where, $\boldsymbol{x}$ is the exemplar pixel vector, $\widehat{\boldsymbol{\mu}}$ a window mean vector, S the window covariance matrix and N the number of pixel vectors in the processing window (Smetek, 2007). As N approaches infinity, Equation (5) converges to the Mahalanobis distance (MD):

$$MD(\boldsymbol{x}) = (\boldsymbol{x} - \widehat{\boldsymbol{\mu}})^T \mathrm{S}^{-1} (\boldsymbol{x} - \widehat{\boldsymbol{\mu}}) \tag{6}$$

with variables the same as Equation (5). For the remainder of the document MD will be referred to as RX. Therefore, the RX detector essentially measures the distance between the pixel under test and the estimated background mean using the estimated covariance matrix of the current processing window (Smetek, 2007).

RX scores are then compared to a given threshold, T_{rx}, and if RX is greater than T_{rx}, the pixel is labeled as an anomaly. T_{rx} is based on the χ^2-distribution with p degrees of freedom and p is the dimensionality of the data (Smetek & Bauer, 2008).

In addition to the previously stated limitations of local anomaly detectors, the RX detector's Gaussian data assumption is not usually a good fit to the data and leads to the aforementioned false alarms issues. Additionally, estimating a background probability

density function for large dimension HSI data is difficult since the sample size increases exponentially with the number of spectral bands (Amit Banerjee & Meth, 2007).

The primary limitation of the RX detector is proper processing window size selection. For a reasonable estimate of the covariance matrix, the processing window must contain at least as many pixels as the number of dimensions of the image (Smetek, 2007). If the number of pixels is less than the dimensions, the inverse covariance matrix will be ill-conditioned and unstable. A general-rule-of-thumb for the number of pixels is about ten times the number of bands (Borghys & Perneel, 2010). Additionally, Borghys and Perneel (Borghys & Perneel, 2010) compare three different methods of work to improve the ill-conditioned and unstable limitation of the RX detector: 1) Prior Principal Component Analysis, 2) Diagonal Loading (DL), and 3) Singular Value Decomposition. Their results suggest that DL give the best results with respect to anomaly detection percentage in most scenarios.

Other RX-based detectors that also attempt to correct these limitations include (Smetek & Bauer, 2008): (Chang & Chiang, 2001), (Hsueh & Chang, 2004), (Riley, Newsome, & Andrews, 2004), (Kwon & Nasrabadi, 2005), (Gaucel, Guillaume, & Bourennane, 2005), (Schaum, 2004), (West, Messinger, Ientilucci, Kerekes, & Schott, 2005), and (Schaum, 2006).

Global Anomaly Detector

Unlike the local anomaly detector where each image pixel is compared to only background pixels within the current processing window, the global anomaly detector attempts to model the entire image background and then test each pixel to determine if it is an anomaly (Smetek, 2007). With this approach theoretically it is better at detecting large, multi-pixel anomalies and decreases the probability of false alarms due to scene clutter (Smetek & Bauer, 2008). Similar to the local anomaly detector, the global anomaly detector also has issues with isolated anomlaies in an open region; however, this

occurs when the anomaly spectral signature is similar to that of the background signature (Stein *et al.*, 2002).

Autonomous Global Anomaly Detector

Recently developed by Johnson (Johnson, 2008), a global anomaly detector is the Autonomous Global Anomaly Detector (AutoGAD). AutoGAD is made up of four phases: Feature Extraction I, Feature Extraction II, Feature Selection, and Identification. The first phase uses PCA as a dimensionality reduction tool (Johnson, 2008). Its goal is to create linear combinations of the original data variables that account for as much variability as possible. The linear combinations created by PCA are orthogonal to each other and account for successively smaller amounts of the total variation in the data. The first principal component (PC) accounts for the most variation (Dillion & Goldstein, 1984).

The second feature extraction phase uses Independent Component Analysis (ICA) to further project the data to a new orthogonal and statistically independent subspace. Within this new subspace, phase three chooses features that correspond to anomalies based on statistical considerations, such as kurtosis. Finally, the pixels are identified as targets based on the features selected (Johnson, 2008). For more information regarding other global anomaly detectors see Smetek and Bauer (Smetek & Bauer, 2008), Madar *et al.* (Madar *et al*., 2009), and Rosario (Rosario, 2006).

Region of Interest Generator

A region of interest (ROI) is essentially a pixel or set of pixels in a hyperspectral image in which a potential anomaly has been detected. For this study we will assess the local anomaly detector RX and the global anomaly detector AutoGAD for the ROI generators. Because the purpose of this study is to develop a baseline ATR, in the future

a different local anomaly detector could be used in their place to assess for possible ATR improvement.

Classification

Classification "is the process of assigning a label to an observation (usually a vector of numerical values)". Classifiers can be characterized as either "hard" or "soft." A hard classifier assigns only one label to each image pixel whereas a soft classifier assigns multiple labels to each pixel (Shaw & Manolakis, 2002).

Recall there are two types of target detection algorithms for hyperspectral imaging data. Classification falls into the category of spectral matching detection algorithms (Manolakis, Lockwood, Cooley, & Jacobson, 2009). Spectral matching, unlike anomaly detection, requires the presence of one or more known reference signatures for the target of interest. Reference signatures usually come from a spectral library created in a laboratory and/or field experiments which are measured in the reflectance spectrum because they do not contain atmospheric conditions (Eismann, 2011) (Manolakis, Lockwood, Cooley, & Jacobson, 2009). The reference signature can also come from an identified in-scene target pixel or a radiance spectrum measured from a different image (Manolakis, Lockwood, Cooley, & Jacobson, 2009) (Eismann, 2011). In the prior case, atmospheric compensation converts from radiance spectrum to a comparable reflectance spectrum by adding the estimated missing atmospheric component (Eismann, 2011).

Anomalous pixels detected from the ROI generator are compared to the reference signature(s) to see if there is a "match." If there is a high degree of correlation a label is assigned to that pixel, or group of pixels (Manolakis, Lockwood, Cooley, & Jacobson, 2009). This matching can be completed using various algorithms (Eismann, 2011) (Manolakis, Lockwood, Cooley, & Jacobson, 2009).

Matched Filter

A basic form of a matched filter (MF) with regards to global statistics is (Eismann, 2011),

$$MF = (\boldsymbol{s} - \boldsymbol{\mu_b})^T \Sigma_{\mathrm{b}}^{-1} (\boldsymbol{x} - \boldsymbol{\mu_b}) \tag{7}$$

where, $\boldsymbol{s}$ is the known vector reference signature, $\boldsymbol{\mu_b}$ the mean vector of the background, Σ_b the covariance of the background and $\boldsymbol{x}$ the pixel (target) of interest. The dimension of $\boldsymbol{\mu}$ and $\boldsymbol{\Sigma}$ is *p*, number of frequency bands. Unknown parameters, $\boldsymbol{s}$, $\boldsymbol{\mu_b}$, and Σ_b typically need to be estimated (Manolakis & Shaw, 2002) (Manolakis, Lockwood, Cooley, & Jacobson, 2009). One typical estimation technique is to calculate $\boldsymbol{\mu_b}$ and Σ_b based on the entire image, called global estimation (Eismann, Stocker, & Nasrabadi, 2009). Obviously, there are issues with this technique if the image has a large number of spectrally different objects as the estimate(s) will be skewed. Other techniques used for background mean and covariance estimation include local and block-wise (Eismann, Stocker, & Nasrabadi, 2009). Similar to the RX detector, the MF is a measure of the distance between the pixel of interest and the known reference signature. Generally speaking a high MF score is a similarity measure of $\boldsymbol{s}$ and $\boldsymbol{x}$. A threshold can then be applied to compare the MF score to. If the score is above the threshold a "match" is made and if the score is below the threshold a "match" is not made.

Adaptive Matched Filter

Another spectral matching algorithm is the adaptive matched filter (AMF) which was originally proposed by Robey *et al.* (Robey, Fuhrmann, Kelly, & Nitzburg, 1992). When dealing with local statistics, as with the RX detector, a modification should be applied (Eismann, 2011). This modified equation is,

$$AMF = \frac{[(\boldsymbol{s} - \boldsymbol{\mu_b})^T \Sigma_{\mathrm{b}}^{-1} (\boldsymbol{x} - \boldsymbol{\mu_b})]^2}{(\boldsymbol{s} - \boldsymbol{\mu_b})^T \Sigma_{\mathrm{b}}^{-1} (\boldsymbol{s} - \boldsymbol{\mu_b})} \tag{8}$$

The data elements of the AMF are the same as Equation (7), with normalization included. The AMF was used for this study because during initial ATR development MF scores were not as high as expected for true anomalies. This will be discussed in more detail in Ch. III, Step 2.

Out-of-Library Decision

Once a pixel vector, or set of pixel vectors, has been labeled as an anomaly and a spectral "match" has been made it will be run through an OOL detector. An OOL label is given to an anomaly that does not closely resemble at least one of the objects within the target library (Friend, 2007). The target library is made up of different classes from targets the detector has been trained to recognize. The difficulty in developing this class library is the inability to classify every known target. On the other hand, if an anomaly resembles an object within the target library an in-library (IL) label is given (Turnbaugh, 2009) (Leap, 2008).

In the literature there are a number of different OOL detector methodologies. These methodologies can be divided into three categories (Friend, 2007).

1. *Transparent* Method is based on complete knowledge of all anomaly classes.
2. *Semi-Blind* Method is based on partial knowledge of the anomaly classes. For instance an OOL label would be decided upon descriptive statistics of the anomaly.
3. *Blind* Method is based on IL objects, no prior knowledge of the anomaly class and anomaly characteristics.

For this study we will simply focus on the use of a threshold for an OOL decision, such a method is considered blind because no *a priori* knowledge of the anomaly classes is required. Once a matched filter score is obtained it is compared to a given threshold. If the filter score is less than the threshold the pixel of interest is given an OOL label. Conversely, if the pixel of interest's filter score is greater than or equals the threshold an IL label is given. As with the RX detector, this method and the following MD OOL method could be replaced with a different method to assess the ATR for possible improvement.

Another OOL method uses the MD score, Equation (6), to identify an anomaly as out-of-library. Similar to the threshold technique, the MD is a Blind method. Comparable to Equation (6), the MD equation can be written as,

$$d_i = (\boldsymbol{x} - \widehat{\boldsymbol{\mu}}_{\boldsymbol{i}})^T C_i^{-1} (\boldsymbol{x} - \widehat{\boldsymbol{\mu}}_{\boldsymbol{i}}) \tag{9}$$

The difference here is C is the covariance matrix for target i, for targets one to i. Therefore, the OOL detector also measures the distance between the pixel under test, $\boldsymbol{x}$, and the estimated class distribution mean, $\widehat{\boldsymbol{\mu}}_{\boldsymbol{i}}$, and estimated class covariance matrix, C. The MD is then compared to a given threshold, T_{md}. If the MD is less than the threshold an OOL label will be given to $\boldsymbol{x}$.

Unfortunately the MD is quite sensitive to outliers, even just one outlier; Smetek (Smetek, 2007) explains three different types of issues that can occur when outliers are present in data: 1) breakdown point, 2) masking effect, and 3) swamping effect. The breakdown point of an estimator is the fraction of outliers that can be present in a sample before the estimator values are meaningless. The masking effect occurs when a very strong outlier distorts a non-robust mean and covariance estimates so much that a weak outlier does not appear as an outlier in regards to the Mahalanobis distance. Finally, the

swamping effect occurs when an outlier distorts the mean and covariance estimates such that even a non-outlier is incorrectly labeled as an outlier. Two basic remedies to these issues involve using robust mean and covariance estimates and the use a different OOL method not based on the Mahalanobis distance if outliers are suspected. Additional OOL methods are described by Albrecht (Albrecht, 2005), Friend (Friend, 2007), and Turnbaugh (Turnbaugh, 2009).

Non-Declaration Decision

After a pixel is declared an anomaly, a matched filter score has been given, and if it has been declared IL, a declaration (DEC) or NDEC decision can be made. A NDEC decision is a label given to an object (or in our case an anomaly pixel vector) such that its spectral signature is similar to more than one other object represented in the library of known objects (Friend, 2007).

For this study the NDEC decision will also be based on a threshold. Here a difference will be taken between the two highest matched filter scores for the anomaly. This difference will then be compared to the threshold. If the matched filter score is greater than or equals the threshold, the pixel of interest can be declared as a specific target. If the score is less than the threshold, a NDEC label will be given as the closeness in matched filter scores would indicate the pixel of interest too closely resembles two different target classes. For the rest of this section, we will briefly touch on previous work completed in the area of non-declarations, to include the NDEC procedure developed by Turnbaugh (Turnbaugh, 2009).

The first method by Chow (Chow, 1970) stated that by reducing the number of objects to be classified due to difficulty in label assignment can actually improve classification accuracy. Based on an optimum rule for rejection, a NDEC label would be given if the maximum of a set of posterior probabilities is less than some threshold T.

The number of posterior probabilities is based on *N* different given classes. In equation form this is described as

$$x \notin w_i \quad \text{if} \quad \max_{k \in 1,2,\ldots,N} P(w_k|x) = P(w_i|x) < T \tag{10}$$

where w_i is the (winning) posterior probability for class *i*, *x* the current exemplar, $P(w_i|x)$ the max posterior probability for class *i* given *x*, and $T \in [0, 1]$ (Chow, 1970).

Then in 2000, Fumera *et al.* (Fumera, Roli, & Giacinto, 2000) expanded on this method where there is a threshold for each class, θ_i. Thus the new equation for a NDEC label is

$$\max_{k \in 1,2,\ldots,N} \hat{P}(w_k|x) = \hat{P}(w_i|x) < \theta_i \quad \text{where} \quad \theta_i \in [0, 1] \tag{11}$$

where the other equation elements are similar to Equation (10). A NDEC decision label is given if the maximum of a set of posterior probabilities is less than the class threshold, θ_i. The rationale that Fumera *et al.* introduce for the improvement was if Chow's assumption of perfect posterior probabilities was violated, no one threshold could be used to find an optimal decision threshold (Turnbaugh, 2009).

Two other methods, Laine (Laine, 2005) and Albrecht's (Albrecht, 2005) were centered on a window-based NDEC method where the window serves as a rejection region. The rejection window is based on a ROC curve analysis. For example, Figure 7 depicts a two class problem where the rejection region is labeled θ_{REJ}. Based on the ROC curve analysis if a θ score falls within the θ_{REJ} region a NDEC label is given. If a θ score is between 0 and 1 and not within θ_{REJ}, a label can be given. For this example a score between θ_{up} and 1 indicates the target is labeled "T." If the score is less than θ_{low} and greater than 0 an "F" label is given.

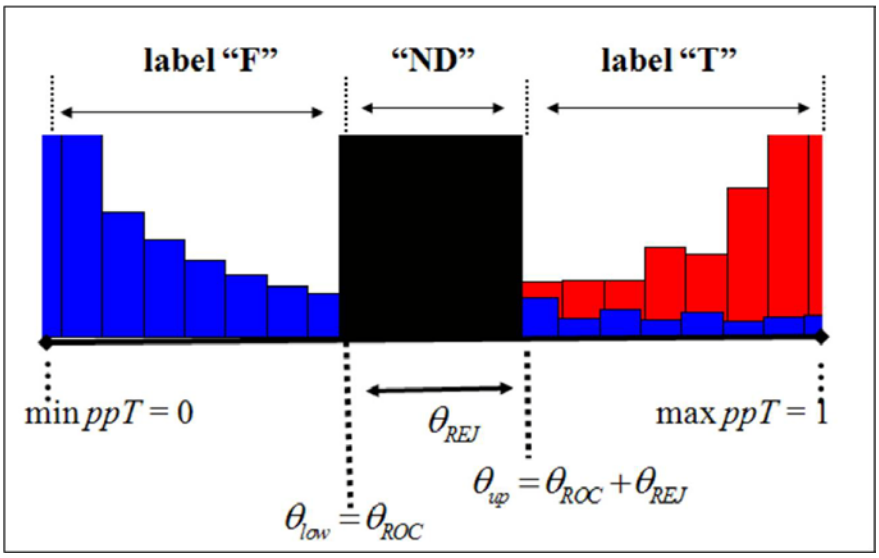

Figure 7. Example Rejection Region for Two Class Problem, taken directly from (Laine, 2005)

An alternative to Laine (Laine, 2005) and Albrecht's (Albrecht, 2005) methodologies is one developed by Friend (Friend, 2007). Friend developed metrics that are based on entropy and Kullback-Lieber distance as NDEC methods (Friend, 2007).

Turnbaugh (Turnbaugh, 2009) extends on the works of Fumera *et al.* (Fumera *et al.*, 2000) and Friend (Friend, 2007) for his method of NDEC. For the current exemplar ***x*** a classification decision is not made if

$$\max_{k\in 1,2,\ldots,N} \hat{S}_\alpha(w_k|x) = \hat{S}_\alpha(w_i|x) < \theta_{i\alpha} \tag{12}$$

where $\hat{S}_\alpha(w_k|x)$ is the estimated similarity measure for class *i* given *x* at aspect angle α.

However, as stated at the beginning of this section, NDECs occur when the object in question resembles more than one object in the library. Therefore, Turnbaugh (Turnbaugh, 2009) used a threshold of the difference between the winning class

similarity measure and the class with the next best similarity measure. The descriptive equation is

$$\max_{k\in 1,2,\ldots,N} \hat{S}_\alpha(w_i|x) - \max_{k\in 1,2,\ldots,N,k\neq i} \hat{S}_\alpha(w_i|x) < \theta_{i\alpha} \quad (13)$$

where $\theta_{i\alpha}$ is a given percentage of the overall range of similarity scores for that exemplar. A detailed example is provided below.

Simply stated, a NDEC label will be given to an exemplar ***x*** if the difference between the winning class similarity measure and the similarity measure of the second best class is less than some percentage of the overall range of similarity measures. For example, for the similarity metric vector

$$S = (0.45, 0.40, 0.10, 0.01, 0.01, 0.01, 0.01, 0.01)$$

the top two scores are 0.45 and 0.40 for class 1 and class 2, respectively. For a 10% non-declaration, $\theta_{i\alpha}$ = (0.45 – 0.01)*0.10 = 0.04. With a top-two score difference of 0.05, we have $0.05 \not< 0.04$; therefore, a declaration can be made. If a 20% non-declaration is used $\theta_{i\alpha}$ = (0.45 – 0.01)*0.20 = 0.09. Because this is larger than the top-two difference a NDEC would be given to this exemplar.

Turnbaugh (Turnbaugh, 2009) then goes on to provide a couple areas where his NDEC methodology differs from the methodology of Friend (Friend, 2007). First, the NDEC decision will be based on how the exemplar compares to each object in the library and not on how other exemplars have compared to the library objects. Second, because posterior probabilities have been negatively criticized in classification systems due to prior probability estimations, Turnbaugh's method does not require posterior probability estimates. Also, the posterior probability estimates are always normalized to sum to 1. According to Richard and Bray (Richards & Bray) and Ross and Minardi (Ross & Minardi, 2004) this is not always a good thing when a forced decision is made.

III. Methodology

This chapter will first discuss the performance measures used for assessments followed by a detail description how the proposed ATR process was developed. The chapter will concluded with a summary of the specific ATR aspects and settings used for the final analysis discussed in Chapter IV.

Performance Measures

The first performance measure used to assess ATR performance is the True Positive Fraction (TPF). TPF is the proportion of correctly classified anomalies; this is calculated with the fraction number of correctly classified true anomalies ("TP count") divided by "TP count" summed with the number of incorrectly classified true anomalies ("FN count"), Equation **(14)**. "TP" stands for "true-positive" and "FN" stands for "false negative." Ideally, the TPF value is equal to or as close to one as possible (Fawcett, 2001)

$$TPF = \frac{TP\ count}{TP\ count + FN\ count} \tag{14}$$

The second measure is the False Positive Fraction (FPF); it is defined as the proportion of falsely classified anomalies. This is calculated with the fraction number of incorrectly classified non-anomalies ("FP count") divided by number of correctly classified non-anomalies ("TN count") summed with "FP count," Equation (15). "FP" stands for "false-positive" and "TN" stands for "true negative." The FPF value is ideally equal to zero or as close to zero as possible (Fawcett, 2001)

$$FPF = \frac{FP\ count}{FP\ count + TN\ count} \tag{15}$$

In order to compare the TPF rates and FPF rates together for each ATR procedure, a variation of a ROC curve is applied. ROC curve analysis is widely used in summarizing imperfect diagnostic system performance, for example ATR and biomedical research (Alsing, Bauer, & Oxley, 2002). A typical ROC curve summarizes the relationship between the TPF and FPF when a variable, or decision threshold, is varied. Figure 8 is a typical ROC curve, where "probability of detection" refers to TPF and "probability of false alarm" refers to FPF; "conservative" and "aggressive" refer to the level at which the decision threshold is varied (Alsing, Bauer, & Oxley, 2002).

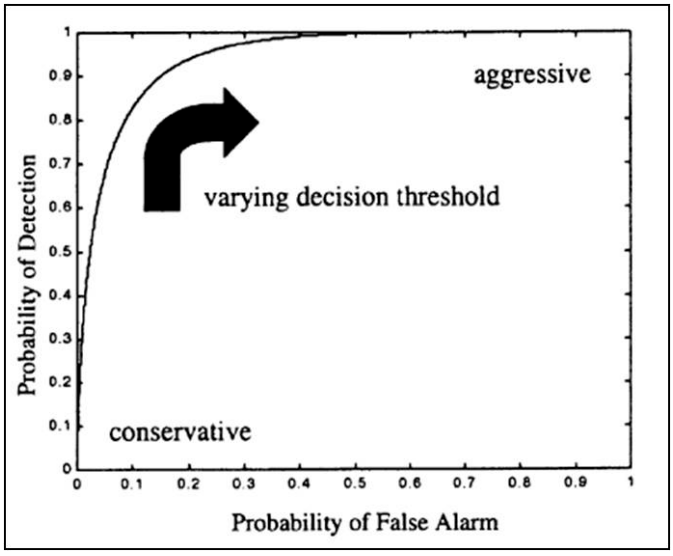

Figure 8. Typical ROC Curve, taken directly from (Alsing, Bauer, & Oxley, 2002)

For this study, instead of varying one decision threshold we will be varying two: OOL threshold and NDEC threshold. Therefore, the curve that is depicted in Figure 8 will not exist and in its place will be distinctive points based on the various OOL and

NDEC threshold level combinations, Figure 9. The concepts of TPFs and FPFs will be extended to two different cases: Classification and Recognition.

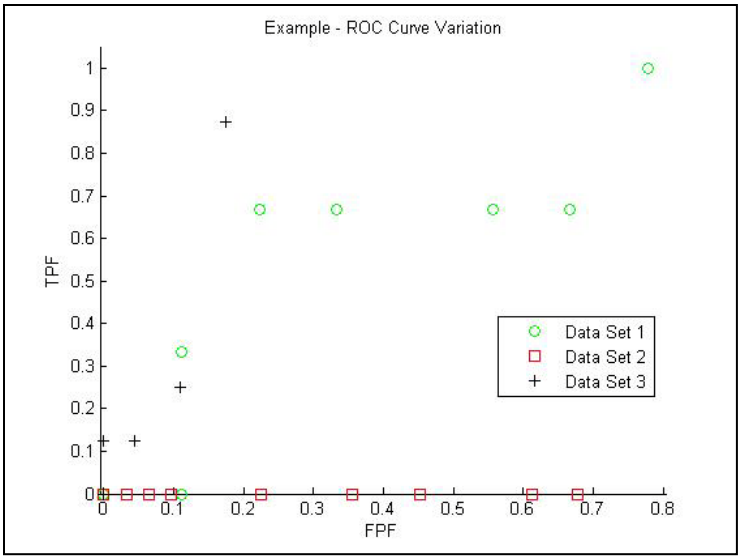

Figure 9. Example ROC Curve Variation

Classification

Classification in this sense corresponds to how an anomaly is identified on a macro-level. The key is that anomalies are either considered a target or background. The anomaly is considered a target if it is identified as one of the targets within the truth library; otherwise, it will be identified as background. Background is defined as anything not within the truth library. A simple confusion matrix is given in Table 1.

Table 1. Classification Confusion Matrix

		Anomaly Identified as…	
		"Target"	"Background"
True Anomaly is…	Target	TP count	FN count
	Background	FP count	TN count

Recognition

Recognition on the other hand corresponds to how an anomaly is identified on a micro-level. For this study we are only considering those anomalies which have made it as a "TP count" from the above section. The key here is that an anomaly is identified as a specific target within the truth library correctly or it is not. In a sense we are dissecting the "TP count" section in Table 1. The recognition confusion matrix is given in Table 2.

Table 2. Recognition Confusion Matrix

		Anomaly Identified as…			
		"Target 1"	"Target 2"	"Target 3"	"Background"
True Anomaly is…	Target 1	TP1 count	FP12 count	FP13 count	FN1 count
	Target 2	FP21 count	TP2 count	FP23 count	FN2 count
	Target 3	FP31 count	FP32 count	TP3 count	FN3 count
	Background	FPB1 count	FPB2 count	FPB3 count	TN count

Because there is more than one target the TPF and FPF calculations need to be considered for each different target. For example, Target 1's TPF and FPF respectively are,

$$TPF1 = \frac{TP1\ count}{TP1\ count + FP12\ count + FP13\ count} \tag{16}$$

and

$$FPF1 = \frac{FP21\ count + FP31\ count}{TP1\ count + FP21\ count + FP31\ count} \tag{17}$$

A similar approach is completed for Target 2 and 3's TPFs and FPFs. The counts for the background labels are given as added information but not used for the target TPF and FPF calculations.

Label Accuracy

The final performance measure is label accuracy. This is described as the percent of anomalies identified as targets that were in fact targets. From the classification confusion matrix the equation is (Fawcett, 2001),

$$LA = \frac{TP\ count}{TP\ count + FPcount} \tag{18}$$

Methodology and ATR Development Process

The methodology can be separated into five different steps: 0) Import image data, 1 a) Region of Interest Generator, 1 b) Atmospheric compensation, 2) Matched Filter, 3) OOL detector, and 4) NDEC decision, Figure 10.

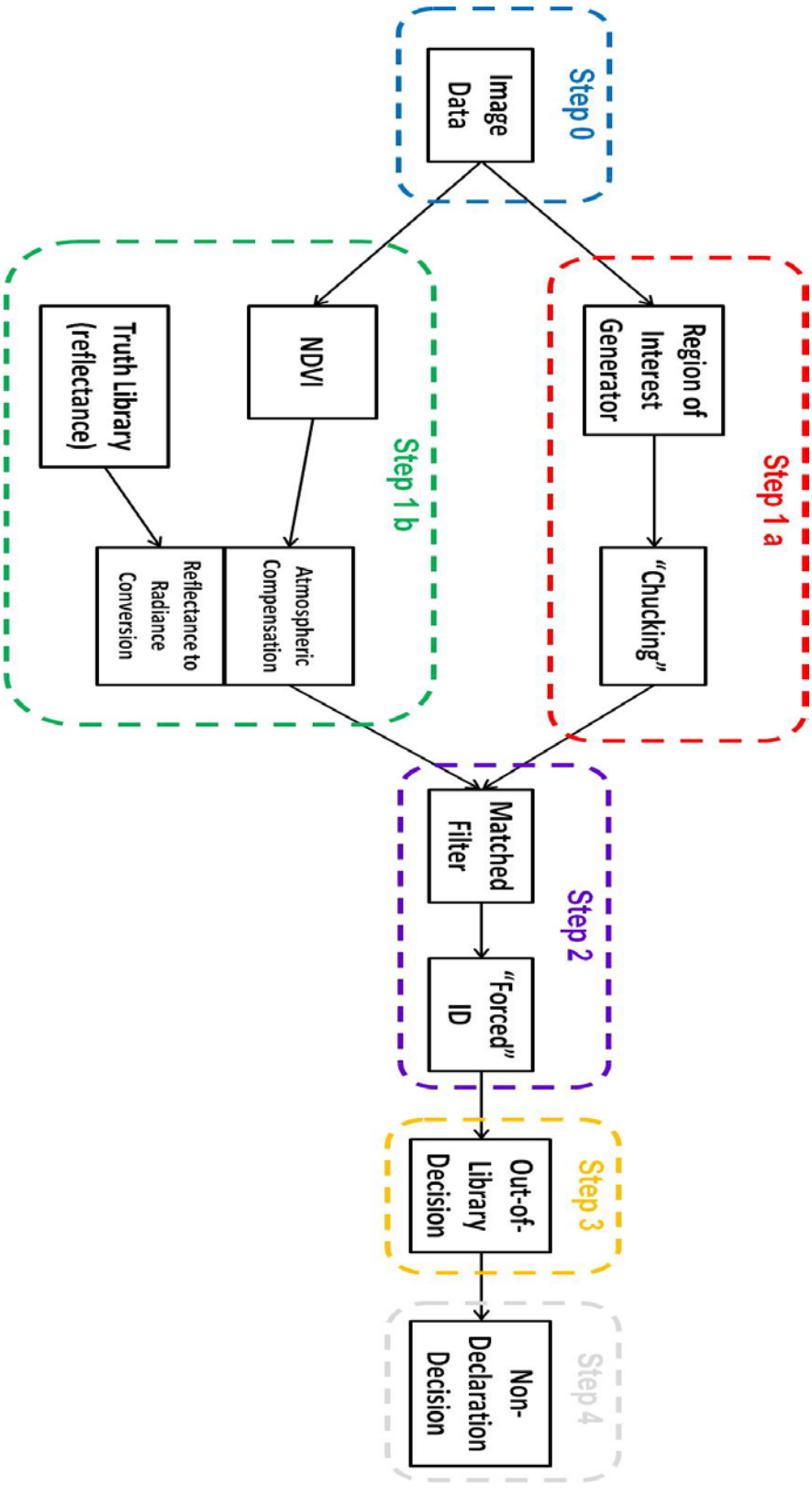

Figure 10. ATR Methodology

Step 0: Import hyperspectral image data

Using the HYDICE data sets, sensor image data, frequency list, and data truth masks are imported. The sensor image data consist of the data matrices, *X*, mentioned in Chapter II. The frequency list contains those frequencies at which the sensor collected image data. Finally, the data truth masks are matrices that indicate the "true" location of image anomalies. The term "true" is used loosely as the data masks were created by hand and are subject to interpretation of the creator of the file.

Atmospheric Absorption

Also included at this step are handling atmospheric absorption bands. These are frequency bands at which the energy emitted from the image is almost completely absorbed by the atmosphere. Any detection in those bands will primarily be random noise (Smetek, 2007). Because these bands provide little information they can be removed from the image data with minimal degradation to ATR performance. For this study the absorption bands are, by observation: 1-9, 98-114, 133-157, and 201-210 (Johnson, 2008). As an example, Figure 11 displays a signature with 210 frequency bands. When absorption bands are removed the signature becomes Figure 12. This process removed data which would corrupt PCA with sensor noise and atmospherically absorbed bands.

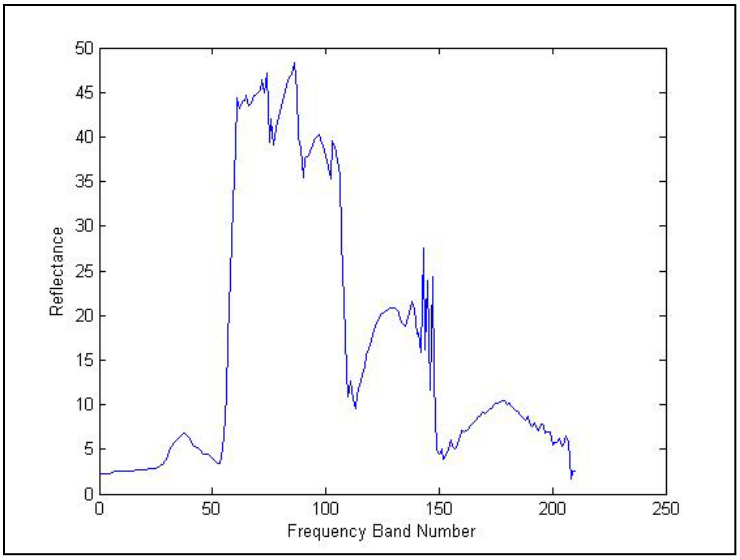

Figure 11. Example Signature Plot with 210 frequency bands

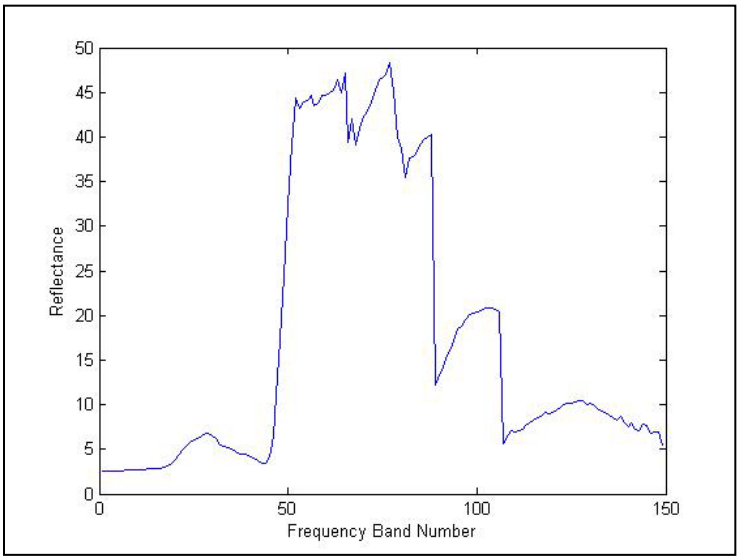

Figure 12. Example Signature Plot without absorption bands

Step 1 a: Region of Interest Generator

Once the image data is imported and absorption bands removed, the image data will then be run through a ROI generator. The original ROI generator used was the RX anomaly detector. As we will see, RX appeared to be miss detect anomalous pixels when compared with the truth

masks; therefore, AutoGAD outputs were examined as well. RX will be discussed first, followed by AutoGAD.

An observational study was completed to determine the effect of the number of PCs retained for the RX detector. RX output files were generated and then graphically depicted to assess the effects of including additional PCs. The RX output is a two-dimensional data matrix containing RX scores for each image pixel. The higher the RX score the more anomalous the pixel in an RX sense. As indicated by the color scale on the right side of Figure 13, low scores are in the blue spectrum and high scores are in the red spectrum. Figure 13 shows that as the number of PCs increase the RX scores actually decrease with regard to the anomalies. Therefore, we see the highest scores for the anomalies when the PCA dimension is only one (second image from the left of Figure 13). A side effect of using less PCs is the background appears to clutter the RX results more. With more PCs the background RX scores decrease, however a performance tradeoff exists with increasing computation time. Two recent studies suggest that the best performance for the RX detector actually occurs around 10 PCs for RX on the HYDICE images (Williams, Bihl, & Bauer) (Taitano, Geier, & Bauer, 2010).

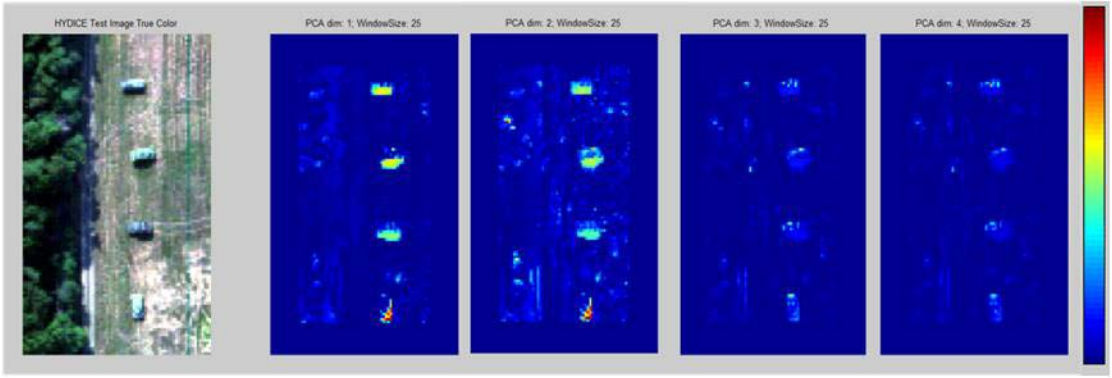

Figure 13. PCA dimensional comparison for RX detector. "PCA dim" equals the number of PCs retained and "Window Size" equals the number of pixels for the length and width of the window.

Another input to be defined for the RX detector is the size of the processing window used to characterize the background pixels. As stated in Chapter II, a general-rule-of thumb in

selecting a window size is 10 times the number of pixels to number of bands (Borghys & Perneel, 2010), or the number of pixels must be at least the number of dimensions of the image (Smetek, 2007). These "rules" were taken into account for the aforementioned observation study to study the effects of window size.

The widow size is defined as the number of pixels for the length and width of the window, i.e., if the window size is 10 this implies the window is actually 10 pixels by 10 pixels. From Figure 14 we see a couple of areas being affected by window size. First, when the window size is small the image produced by the RX detector scores appear cluttered, with no noticeable definition of anomalies, Figure 14 (a). This occurs when the window is small and background estimates appear to closely resemble the center pixel of interest. Second, as the window size increases in size the anomalies become readily apparent with large RX scores. In fact, in Figure 14 (b) there is no mistaking the anomalies. With large windows more accurate background estimates can be calculated and a good RX score can be calculated for the center pixel. Unfortunately, there are more distinguishable "frames" appearing in the images. This is directly due to the increase in window size because the pixels within the frame cannot be estimated because the window size is too large. Based on the suggested "rules", the observational study, and the study by Williams *et al.* (Williams, Bihl, & Bauer), a window size of 25 was utilized, giving a total of 626 pixels per window.

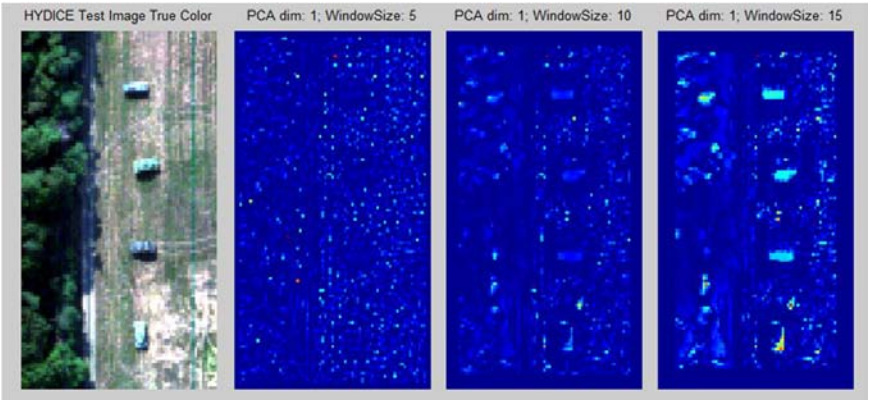

(a)

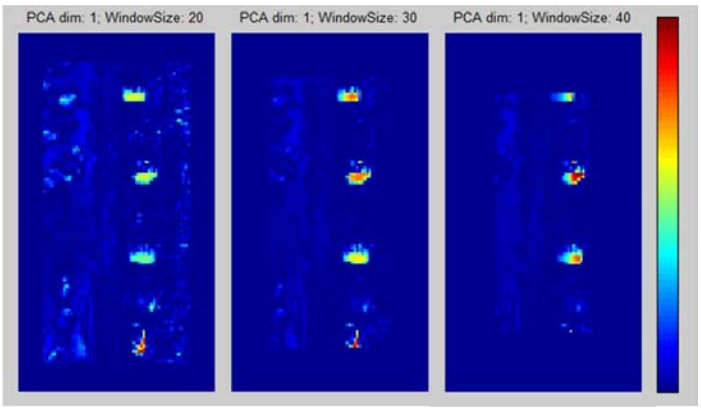

(b)

Figure 14. Window Size comparison for RX detector. "PCA dim" equals the number of PCs retained and "Window Size" equals the number of pixels for the length and width of the window.

In an effort to correct the "framing" issue the Linear RX (LRX) detector was also initially assessed, LRX is a variation of RX (Williams, Bihl, & Bauer). Instead of using a moving window to characterize background pixels, LRX uses a line of pixels above and below the pixel of interest. If the pixel of interest is too close to the upper or lower border and a full line is not complete, the line will extend to the previous column or next column depending on the location of the pixel of interest. A depiction of the LRX moving column is in Figure 15.

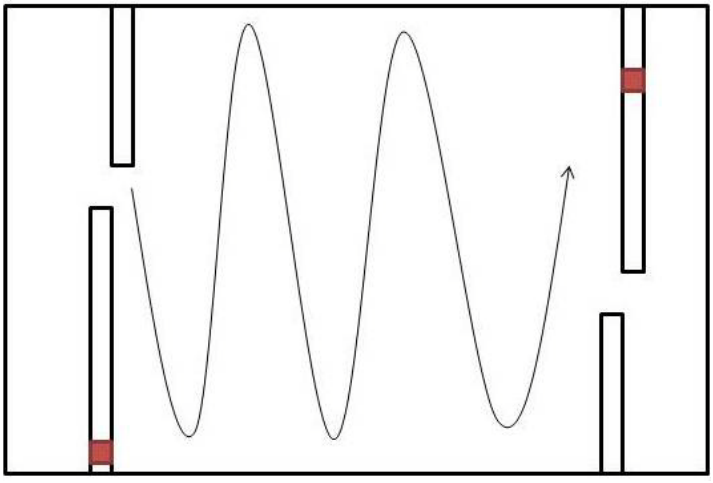

Figure 15. LRX Moving Column Example, taken directly from (Bush, 2012)

LRX images based on scores were observed at varying line sizes, Figure 16. Again, anomalies with high scores are more likely anomalies. A few things become evident by assessing the images. First, the RX issue of "framing" has now been eliminated. Second, there appears to be a greater amount of clutter present. Finally, as the line size increases the anomalies become more noticeable with increased scores, see top anomaly. One noticeable limitation is that if anomalies are vertically aligned, as is the case in Figure 16, when the line overlaps a number of anomalies the LRX score tends to be lower. Similarly, areas along the road on the left of the image where there is tree overhang are highlighted as possible anomalies. Because of the increased clutter in the images it was decided to continue with the regular RX detector as the ROI generator.

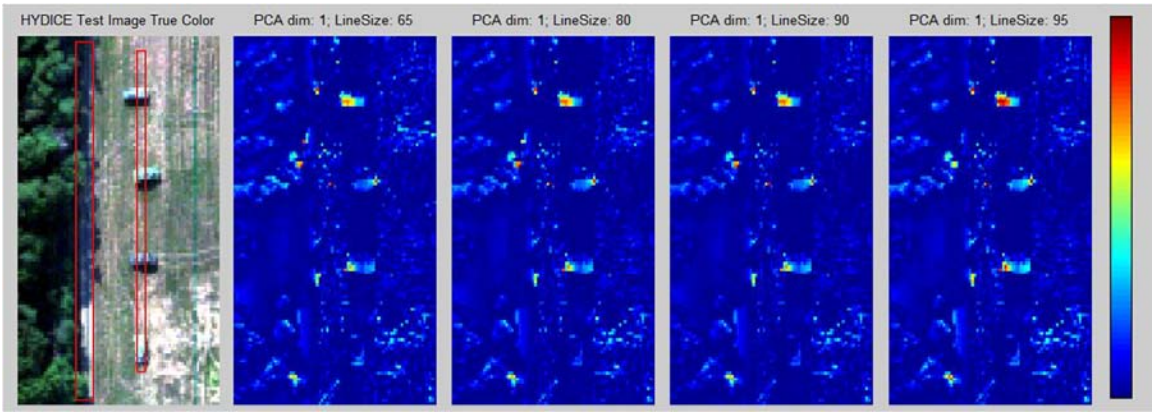

Figure 16. LRX score comparisons based on varying Line Size. Number of PCs equals one.

With the ROI decided upon, the RX detector function is executed and each RX score is compared to a given threshold based on the Chi-squared distribution. Distribution inputs include an alpha value, or the probability that a score is greater than the threshold, and v degrees of freedom, or the dimensionality of the data. Because PCA was completed on the image data the degrees of freedom are the number of PCs retained, which is 10 for this study. If an RX score is greater than the threshold a one is recorder in the corresponding cell in a new matrix of binary

indicator variables representing an anomaly; otherwise, the corresponding cell is set equal to zero representing background.

In the observation study several alpha values were assessed. From Figure 17 it is obvious that as the alpha value decreases the number of potential anomalies (labeled "Number of Categories" on the image) also decrease. This is because as the Chi-squared value increases due to smaller alpha values, less noise will be detected as an anomaly. The number of categories is defined using the "regionprops" command in MATLAB where each spatially separated pixel is a different category. If a pixel is touching another pixel to the left, right, top, bottom, or diagonally they are grouped into the same category. A downside of a small alpha can be the computation time but we found that to be negligible and thus an alpha of 0.01 was decided upon. It should be noted that Figure 17 actually used one PC.

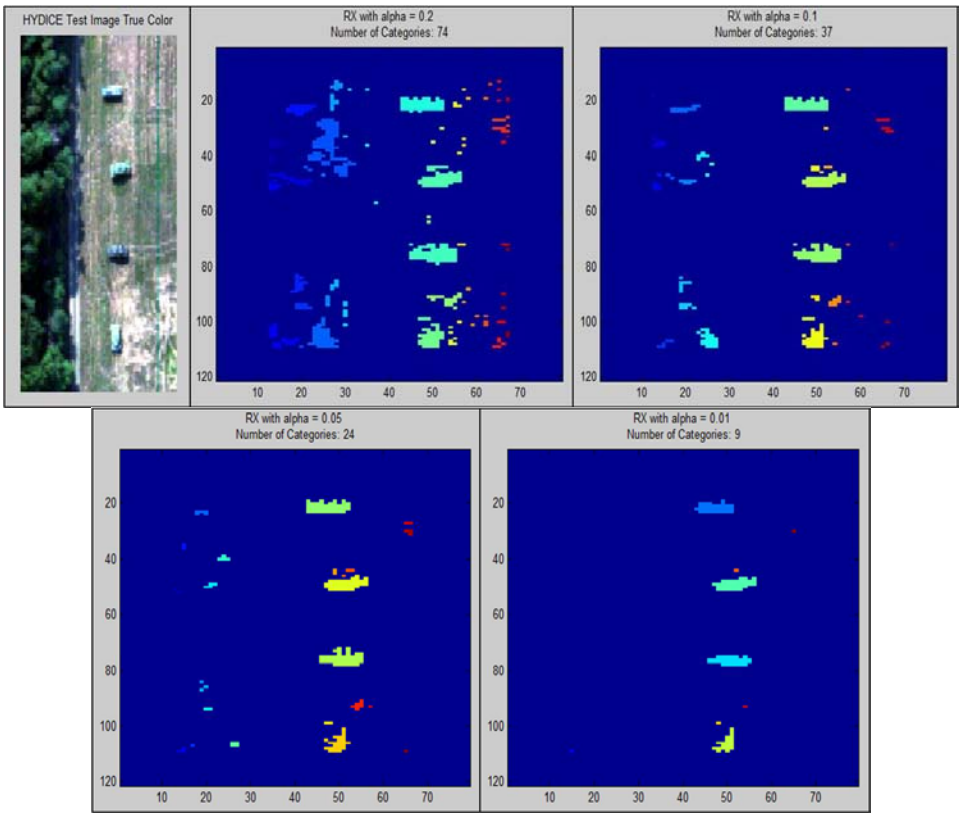

Figure 17. Alpha Value Comparison for RX Detector

Following the grouping of anomalies a simple heuristic, called “Chucking,” was used to decrease the number of potential anomalies to be assessed in the remainder of the ATR process. Chucking is simply removing potential anomalies based on the number of pixels that make up the anomaly group. It was assumed that anomaly groups containing three or less pixels were erroneous, and therefore removed. By applying the chucking heuristic the number of categories decreased to a more manageable level when compared to levels without chucking applied. Figure 18 shows the results of chucking when applied to the images in Figure 17. The result of the chucking heuristic is summarized in Table 3.

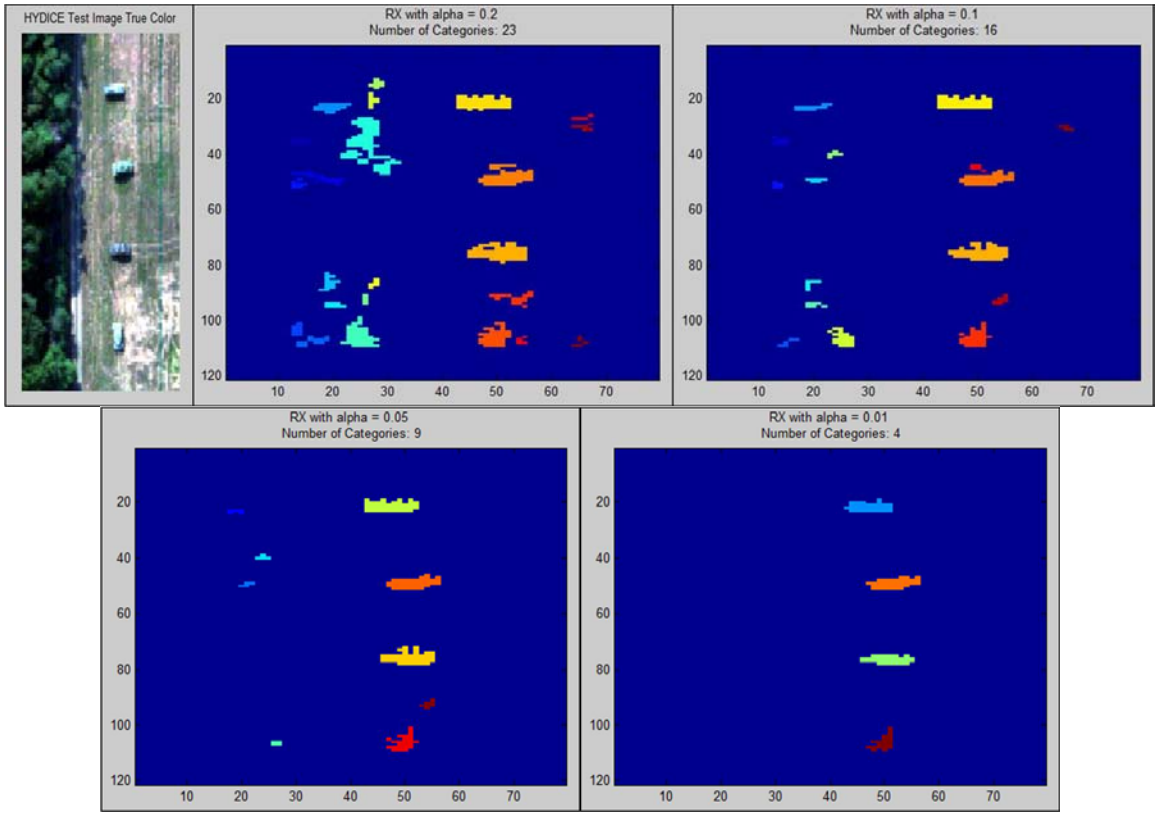

Figure 18. Chucking Hueristic results when applied to RX detector

Table 3. Number of Categories (anomaly groups) with or without Chucking per RX alpha level.

RX alpha level	Without Chucking	With Chucking
0.20	74	23
0.10	37	16
0.05	24	9
0.01	9	4

Due to the known limitations of the RX anomaly detector (specifically the "border" issue) and the matched filter performance results observed in Step 2 below, the global anomaly detector AutoGAD was also considered. Unlike RX, AutoGAD outputs if a pixel was an anomaly or just background, Figure 19. Also, while there are thresholds inherent to AutoGAD the settings from Johnson (Johnson, 2008) were used for this study. The main reason behind the investigation between ATRs with RX and AutoGAD came to fruition because it was noticed during initial ATR assessments that ROC curves for the RX ATR appeared to outperform the AutoGAD ATR, Figure 20. This is of interest because AutoGAD was shown to be an improved anomaly detector and it was unexpected that an ATR with RX would perform better (Johnson, 2008). It should be noted that the vegetation index threshold in Figure 20 will be addressed in the next section.

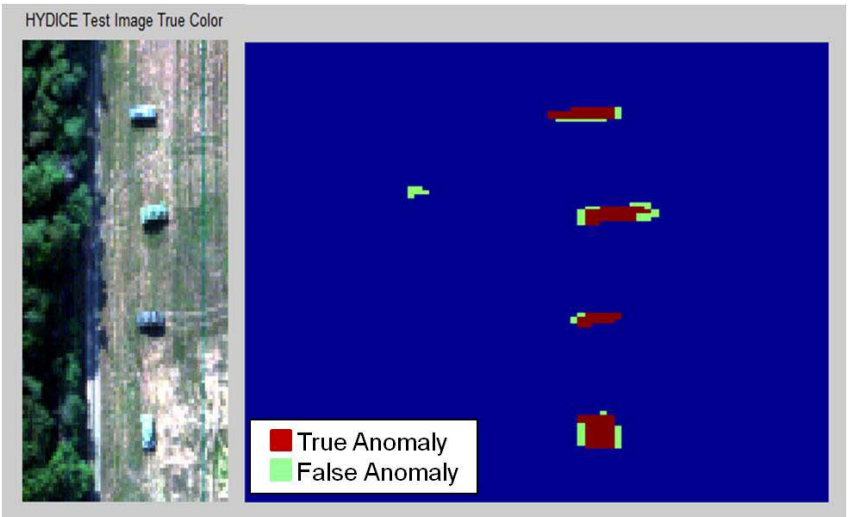

Figure 19. Example AutoGAD Output

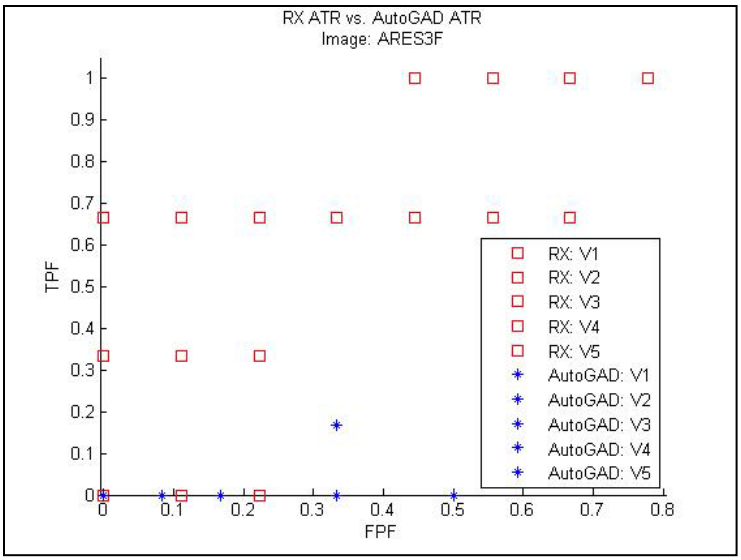

Figure 20. ROC comparison of RX (alpha = 0.01 and 1 PC) and AutoGAD per different Vegetation Index Threshold (V1 – V5)

Step 1 b: Atmospheric Compensation

To deal with the unknown illumination and atmospheric conditions present in all HSI images and to convert reflectance data to radiance data the linear approximate, Equation (1) was applied. NDVI was used to locate healthy vegetation; other estimates were used to calculate the "known" reference signatures required for the gain and offset parts of the approximate. Recall that ELM was not used exclusively because locating the known reflectance signatures could not be automated and did not meet a study objective of a fully automated process.

Normalized-Difference Vegetation Index

The NDVI equation, Equation (4), requires the L_p(860 nm) and L_p(660 nm) values for each pixel. Because spectral sampling is not exactly at whole numbers of wavelengths, the nearest values can be obtained by first subtracting the desired wavelength from each of the frequencies listed in the HYDICE frequency list. Next, the absolute values of the differences are taken. Finally, the minimum value is extracted giving the location of either band, indicating the closest value to the desired wavelength. The result gives the location of the red and NIR bands

with respect to the image being processed. Next, the NDVI is calculated for each image pixel. Figure 5 (b) is an example display of the NDVI values.

Because only high values are considered healthy vegetation, each value is compared to a given threshold. This threshold is subject to the results of the NDVI values for each image. Consequently, a quick study was completed to see if there was an optimal vegetation index threshold based on a percentage of images pixels assumed to be healthy vegetation. The study looked at five different percentages of image pixels: 0.5, 1.0, 5.0, 10.0, and 20.0. These percentages will be referred to as vegetation indices. For each percentage the number of pixels to retain was calculated. The NDVI value for each pixel is reshaped into a vector and is sorted from largest to smallest. The top numbers of retained pixels are kept and the minimum NDVI value is recorded. This minimum NDVI value serves as the vegetation index threshold. For example, Table 4 lists NDVI values from largest to smallest. The NDVI value 0.192 is the minimum value of the top 5% of image pixels per NDVI score. Therefore, 0.192 is the vegetation index threshold for this example.

Table 4. Example Vegetation Index Threshold

NDVI Values	0.201	0.197	…	0.195	0.192	0.188	…	-0.155	-0.162

Top 5% NDVI values

Assessment of the vegetation index levels was completed with a review of ROC curves based on TPF and FPF scores. Images ARES1D, ARES1F, ARES3D, ARES3F, ARES5, and ARES6D_10kFT were processed through the ATR for this quick study. The remaining images were not processed because they did not contain objects in the truth library. TPF and FPF results were calculated for each combination of vegetation index, 15 OOL thresholds, and 15 NDEC thresholds and were plotted to create ROC curves. All six ROC curves are given in Appendix A,

but for convenience an example is provided in Figure 21. Details on the OOL and NDEC thresholds will be discussed later.

To assess all six images rankings of 1 to 5 were given for each image ROC curve (shown in Figure 21) and summarized in a table similar to Table 5. All tables can be found in Appendix B. The rankings are based on ideal TPF, FPF combinations mentioned earlier. For example, in Figure 21 the vegetation index of 5% would be considered the best and ranked one. Unfortunately, this one location does not include all the OOL, NDEC threshold combinations for vegetation index 5% as scores are also located at rankings 2 and 5 and other unranked locations.

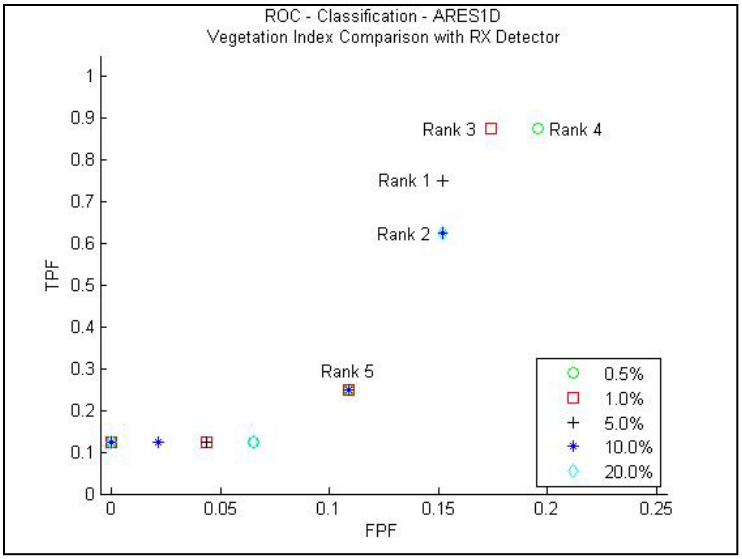

Figure 21. ROC curve for Vegetation Index comparison with RX detector (1 PC) and image AERES1D

Table 5. Vegetation Index ranking assessment for image ARES1D

Image	Ranking	Vegetation Index (%)				
		0.5	1.0	5.0	10.0	20.0
ARES1D	1			1		
	2				2	2
	3		3			
	4	4				
	5	5	5	5	5	
	sum	9	8	6	7	2
	average	4.5	4	3	3.5	2

Originally just the number one rankings were assessed with no clear vegetation index as the one to use. It was then thought that a vegetation index may never get ranked number one but still be the overall best because it scored relatively high on all images. Thus the sum and average of the rankings were taken, Table 5. Unfortunately, it too was inconclusive when looking at just the sums, averages, or a combination of sums and averages. It was also thought that different image types (Forest and Desert) might require different vegetation indices. After review, this too was inconclusive. With the study being inconclusive and due to time limitations a vegetation of 5% was decided upon.

The next step in the NDVI process is to locate those pixels where the NDVI values are greater than the vegetation index threshold. Those pixel's frequencies are then averaged across the frequency bands, resulting in a mean vector that represents the radiance measurement for vegetation. This serves as the first reference signature, L_1, used for the gain and offset calculation in Equations (2) and (3), respectively. The second reference signature, L_2, is referred to as a shade spectrum and is determined by using the minimum radiance value of the image in each frequency band. Figure 22 depicts an example NDVI mean and shade spectrum signatures.

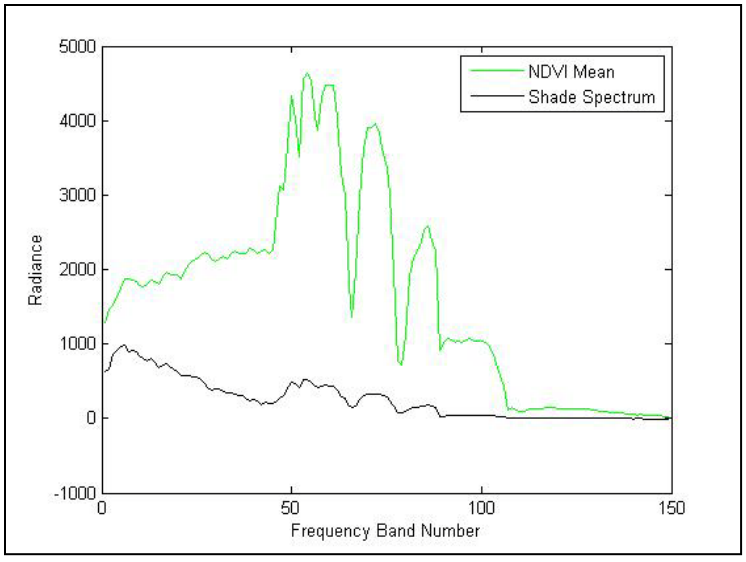

Figure 22. Example NDVI Mean and Shade Spectrum Signatures

Gain and Offset

Recall that L_1 and L_2 from Equations (2) and (3) refer to the known reference signatures (in radiance) provided by NDVI and ρ_1 and ρ_2 are known reflectance signatures. To obtain one of the reflectance signatures an assumption is made that a specific vegetation type available in a truth library is present in the image. In theory this could be any vegetation because of the prior assumption that vegetation reflectance signatures have a distinct shape and most images will contain a fair amount of vegetation (Eismann, 2011). For this study the reflectance signature of the sweet gum tree was selected to serve as ρ_2. Note the absorption bands are removed from the reflectance signature. The other reflectance signature, ρ_1, is simply a zero vector the same dimensions as the sweet gum tree with absorption accounted. With gain and offset equations established, estimates can be calculated and the linear approximate can be completed.

Linear Approximate

The goal of the linear approximate, Equation (1), is to convert a known reflectance signature(s) to an image based, atmospherically compensated radiance signature(s). The reflectance signature(s) is the signature(s) that is available in the truth library. For this study we are focused only on man-made objects to include M1 tanks, T-72 Soviet tanks, and HMMWVs with woodland camouflage. Now that an atmospherically compensated radiance signature exists for each item in the truth library each anomaly (pixel or group) can be statistically compared to the radiance signatures for classification.

Step 2: Matched Filter and Forced Identification

The classification method applied here was the adaptive matched filter (AMF). However, before the AMF was applied the basic form of the matched filter (MF), Equation (7), was assessed. It should be pointed out that the ROI generator for the following assessments was the RX anomaly detector. The MF requires four inputs: a known reference signature (or truth signature), a mean vector estimate of the image background, a covariance estimate of the image

background, and the signature of the anomaly pixel of interest. Each input will be briefly described next.

The known reference signature is the atmospherically compensated radiance signature calculated in Step 1. The mean vector estimate of the image background is the average sensor value for each image pixel across the different frequency bands. The covariance estimate of the image background is the covariance of all image pixels at all frequencies. Note: the MATLAB covariance function removes the mean from each column (frequency band) before calculating the covariance. Finally, the anomaly pixel of interest's signature is the signature that will be tested for classification.

The first pixel of interest signature that was assessed was the average anomaly signature. Recall, after chucking was completed in Step 1a groups of anomalies were given. These groups consist of four or more image pixels. The average anomaly signature used for the MF is the average sensor reading across the frequency bands. Figure 23 is an example of an anomaly group with individual pixel signatures and the average signature plotted.

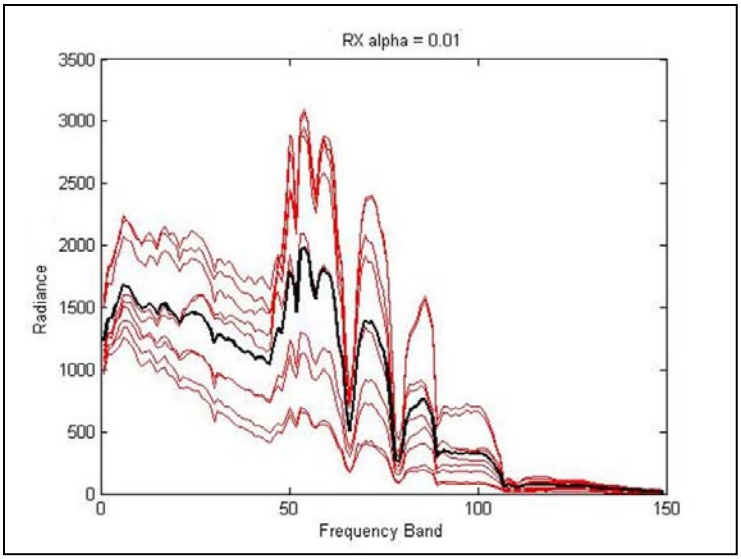

Figure 23. Example Average Signature and Individual Pixels Signature Plot

It was noticed that the MF scores of the anomaly average signatures were not as expected. Anomalies that were within the target library did not score as high as expected, while anomalies outside the target library were scoring rather high. An issue identified when comparing the anomaly group pixel list to the true anomaly pixel list was the two pixel lists were not corresponding very well. In fact, it appeared as if the anomalies detected by the RX detector were focused on the shadows. Therefore, a second signature from a pixel of interest was assessed.

The next signature from a pixel of interest was the centroid of the anomaly group. In practice this was a bad idea. If the anomaly group was of an even number of pixels or of an odd shape the given centroid was rounded. For example, the centroid of the above example was calculated as [63.889, 102.111] and rounded to the nearest whole number, [64, 102]. This cell location was then used as the pixel of interest. This did not perform very well and it was decided that the rounded pixel location could essentially round to a pixel outside of the anomaly group if the anomaly group was not symmetric. Other methods briefly observed were the median signature and the mode signature of the anomaly groups with no advantages noted.

Since MF scores of the known (true) anomalies in the truth library were on the extremely low side it was decided to try the AMF, Equation (8). Additionally, a new technique to determine the signature of an anomaly group was looked at instead of the group average anomaly signature, centroid signature, and other signatures. This technique involved calculating the AMF score of each pixel in the anomaly group for all truth signatures in the library. Then a classification label would be assigned (forced) based on the overall maximum AMF score. The maximum AMF score would then be applied to Steps 3 and 4.

To reach the overall maximum AMF score a data fusion technique was applied. Data fusion was accomplished by counting the number of anomaly pixels that were assigned (forced) to the different library targets. This is easier explained through an example. Table 6 displays the AMF scores for each pixel in anomaly group #3 versus the different library targets; the maximum AMF score is highlighted per pixel. Each maximum AMF score is then counted for

each library target type and plotted in a histogram, Figure 24. The maximum AMF score came from the library target with the highest count. For this example library target five contained the highest count and its maximum AMF score is 6.635.

Table 6. Example AMF Scores with maximum score per pixel highlighted

AMF Scores	Anomaly Group #3								
	Pixel Number								
Library Target	1	2	3	4	5	6	7	8	9
1	0.339	0.355	1.534	0.545	0.508	3.989	0.207	0.099	5.29
2	0.323	0.318	1.218	0.584	0.673	5.299	0.166	0.235	6.76
3	0.337	0.374	1.783	0.483	0.350	2.740	0.238	0.021	3.820
4	0.123	0.693	1.561	0.090	0.099	1.752	0.003	0.138	4.272
5	0.004	0.418	6.635	0.652	1.222	0.608	1.509	1.237	0.626

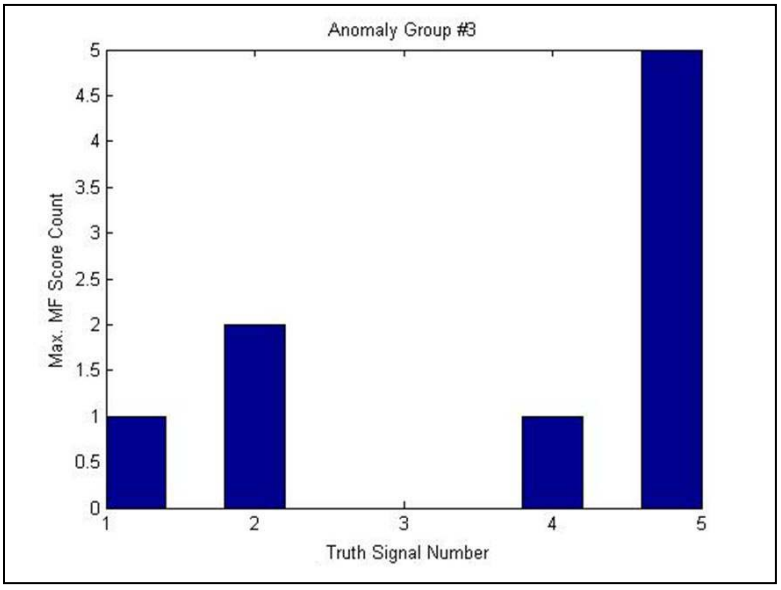

Figure 24. Example Histogram of Maximum AMF Score Count for RX detector

After examination of this “maximum” technique it was noticed that there could exist the possibility for extreme values, or outliers, to skew results. To account for this variability a new “maximum average” technique was applied. To accomplish this, the average AMF score of each library target type was calculated. The assignment (forced ID) of the anomaly group would correspond to the location of the maximum average. Referring to the above example the average of each pixel per library object are given in Table 7 with the maximum average highlighted. Therefore, the forced ID for this anomaly group would be library target type two and the average AMF score, 1.731, which would be passed to Steps 3 and 4 for further assessment.

Table 7. Example Average AMF Scores for Anomaly Group #3 with RX detector and maximum score highlighted

Library Target	Average AMF Scores
1	1.430
2	1.731
3	1.127
4	0.970
5	1.435
ROI: RX with 1 PC and 25x25 Window Vegetation Threshold Index: -0.34	

From Table 7 it is obvious that the “maximum average” AMF scores are still rather low. This was the case for other true anomalies as well. Therefore, it was at this point that AutoGAD was introduced as a ROI generator. The belief was it would detect fewer pixels in the shadow regions and more of the center anomaly pixels. Continuing the same example, the results shown in Figure 25 and Table 8 were promising. The cell count of maximum MF scores per pixel fell in signal number two, Figure 25, which is a target within the target library. The maximum averages have also increased, Table 8. For these reasons AutoGAD was decided upon as an additional ROI generator to assess and the “maximum average” technique would be applied.

Note, Figure 25 indicates anomaly group five and Figure 25 indicates anomaly group three; these refer to the same truth anomaly.

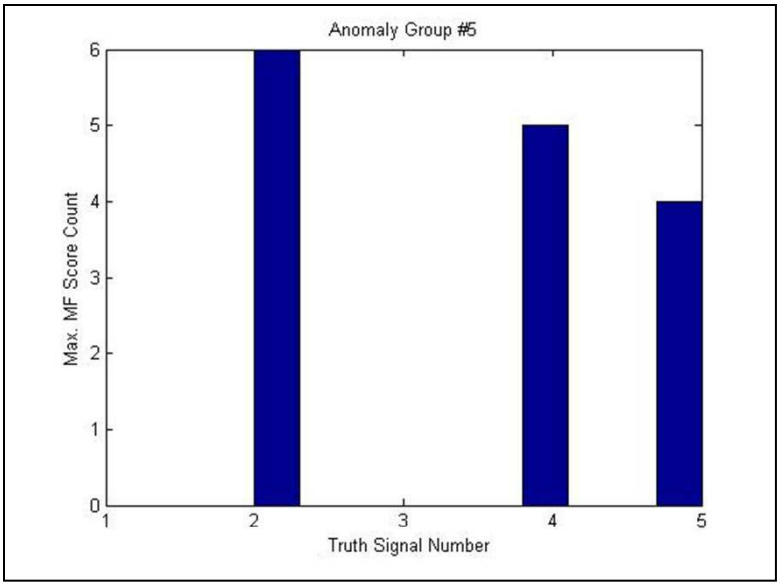

Figure 25. Example Histogram of Maximum AMF Score Count for AutoGAD detector

Table 8. Example Average AMF Scores for Anomaly Group #3 with AutoGAD detector and maximum score highlighted

Library Target	Average AMF Scores
1	4.275
2	4.784
3	3.649
4	4.308
5	1.752
ROI: AutoGAD Vegetation Threshold Index: -0.34	

Step 3: Out-of-Library Detector

With the AMF score decided upon via the "maximum average" technique it will now be compared to thresholds to determine whether the anomaly is labeled as OOL or IL. Because AMF scores are dependent on the image the thresholds could not be hardcoded. To account for

this the maximum AMF was recorded and divided by the number of desired threshold levels. In this case we used a nominal 15 levels. The quotient serves as the minimum threshold value as well as the increment value between threshold levels. The AMF is then compared to each of the thresholds. If the AMF score is less than the threshold an OOL will be assigned, indicating the anomaly does not resemble at least one of the objects within the target library. At this point the object would not proceed to the NDEC decision. On the other hand, if the AMF score is greater than or equals the threshold an IL label will be assigned, indicating the anomaly resembles an object within the target library. Because the anomaly is labeled with an IL the NDEC decision step can be accomplished.

As an example, Table 9 shows the maximum average AMF scores for four anomaly groups, where the third column value (highlighted in green) was the value determined from the previous example. Because 4.784 is the maximum of the maximum average AMF scores, the thresholds are determined by dividing it by the number of desired thresholds. For this example we divide 4.784 by five. Therefore, the minimum threshold is $4.784/5 = 0.957$. This value is also the range between thresholds. Comparing AMF scores to the different threshold levels we are able to determine IL and OOL labels.

Table 9. Example of 5-Level OOL Threshold Comparison

Threshold	Maximum Average AMF Scores per Anomaly Group			
	3.405	4.784	1.945	2.124
0.957	IL	IL	IL	IL
1.914	IL	IL	IL	IL
2.870	IL	IL	OOL	OOL
3.827	OOL	IL	OOL	OOL
4.784	OOL	IL	OOL	OOL

Step 4: Non-Declaration Decision

Assuming the anomaly is labeled as IL in Step 3 the NDEC decision is next. Prior to applying a similar threshold technique as in Step 3, the difference of the two highest AMF scores per anomaly group is calculated. These differences are then compared to the different threshold levels. If the difference is less than the threshold a NDEC label is assigned to the anomaly indicating the anomaly too closely resembles the two different target classes. If the difference is greater than or equals the threshold, the anomaly can be declared as the forced ID in Step 2.

Continuing with the average AMF scores from Table 8, the top two scores are 4.784 and 4.308 with a difference of 0.476. As a five level threshold example of the NDEC procedure, in Table 10 there are four anomaly groups with their respective AMF score differences. Column three (highlighted in green) is the maximum difference, thus the NDEC threshold levels are based on dividing 0.476 by five. When the difference is greater than or equal to the threshold a DEC label can be given; otherwise, a NDEC label is given.

Table 10. Example of 5-Level NDEC Threshold Comparison

Threshold	Difference per Anomaly Group			
	0.302	0.476	0.180	0.257
0.095	DEC	DEC	DEC	DEC
0.190	DEC	DEC	NDEC	DEC
0.286	DEC	DEC	NDEC	NDEC
0.381	NDEC	DEC	NDEC	NDEC
0.476	NDEC	DEC	NDEC	NDEC

Summary

To summarize, the following two ATRs used for assessment and their required settings are given in Table 11.

Table 11. Summary of ATRs and required settings

	ATR 1	**ATR 2**
ROI Generator	RX	AutoGAD
- **Number of PC's**	- 10	- n/a
- **Alpha Level**	- 0.01	- n/a
- **Window Size**	- 25	- n/a
Atmospheric Compensation Technique	VN	VN
Vegetation Index Percentage	5.0%	5.0%
Matched Filter	AMF	AMF
AMF Score Technique	Max. Avg.	Max. Avg.
Number of OOL Thresholds	15	15
Number of NDEC Thresholds	15	15

IV. Results and Analysis

This chapter begins with an explanation of the truth target library, data sets for training and testing, and replication of data. An assessment is then provided for the training images with a final recommendation of OOL threshold and NDEC threshold. Finally, the recommended thresholds are applied to the test data set and the results are assessed.

Truth Target Library

The truth library consists of five different reflectance signatures. Each target's signature is the mean of a number of different individual signature measurements, last column of Table 12.

Table 12. Truth Target Library Data

Target Name	Target Type	Number of Reflectance Signatures
M1	M1 US woodland tank	8
M1	M1 US woodland tank	5
M1	M1 US woodland tank	13
HMMWV	HMMWV US utility vehicle, woodland	5
T-72	T-72 Soviet tank, woodland	8

Training and Testing Data Sets

The images are divided into three groups:

- Group 1: training with library objects,
- Group 2: testing with library objects, and
- Group 3: testing without library objects.

Group 1 images are used to establish the recommended settings for the OOL threshold and NDEC threshold per RX, AutoGAD, and overall. Group 2 images are used to assess the ATR performance. Finally, Group 3 images are used to assess the false-positive rates for images that

do not contain library objects. The images for Groups 1 and 2 were selected at random. The image lists per group and image properties are summarized in Table 13.

Table 13. Training and Test Image Groups and Properties

	Image – ARES	Properties						
		Pixel Dimensions	Number of Targets				Total Targets	Scene Type
			M1	HMMWV	T-72	others		
Group 1	1F	191x160	--	2	4	3	9	F
	3F	226x136	4	3	1	12	20	F
	4	460x78	--	--	3	15	18	D
	5	355x150	4	3	1	7	15	F
	6D_10kFT	215x77	--	--	6	7	13	D
Group 2	1D	291x199	--	--	6	--	6	D
	3D	156x156	--	3	--	1	4	D
	5F	470x155	2	--	--	38	40	F
	7F_10kFT	161x88	--	3	4	4	11	F
Group 3	2D	215x104	--	--	--	46	46	D
	2F	312x152	--	--	--	30	30	F
	4F	205x80	--	--	--	28	28	F
Legend: D – Desert and F – Forest								

Replications

Due to the deterministic nature of the ATR with the RX detector only one run for each image is required. Conversely, the ATR with the AutoGAD detector has a stochastic element caused by the "fastICA" algorithm inherent in the function (Johnson, 2008) (Hyvärinen, 1999). However, operationally if an ATR with an AutoGAD ROI generator was employed the

variability would be taken into account and based on experience the variation is considered negligible (Johnson, 2008). Therefore, ATR assessments with AutoGAD will only include one replication.

Training (Group 1) Data Set Analysis

The purpose of the training data analysis is to decide on the OOL and NDEC thresholds. Training data runs for the RX and AutoGAD ATRs were completed in the following order, Table 14.

Table 14. Group 1 Data Set Run Order

Run Number	ROI Generator	Image	Run Number	ROI Generator	Image
1	RX	ARES3F	6	AutoGAD	ARES3F
2	RX	ARES6D_10kFT	7	AutoGAD	ARES1F
3	RX	ARES5	8	AutoGAD	ARES6D_10kFT
4	AutoGAD	ARES5	9	RX	ARES4
5	RX	ARES1F	10	AutoGAD	ARES4

ATR with RX Anomaly Detector

TPF and FPF results for each combination of OOL threshold and NDEC threshold for the four-step ATR with the RX detector are provided in Figure 26. The optimal FPF is 0.000 and TPF is 0.750. These results occur at OOL threshold levels 7 - 10 and NDEC threshold level one. Coincidently, the OOL thresholds were the same for the three-step ATR. Obviously, there are no thresholds for the two-step ATR. A summary of the results are given in Table 15.

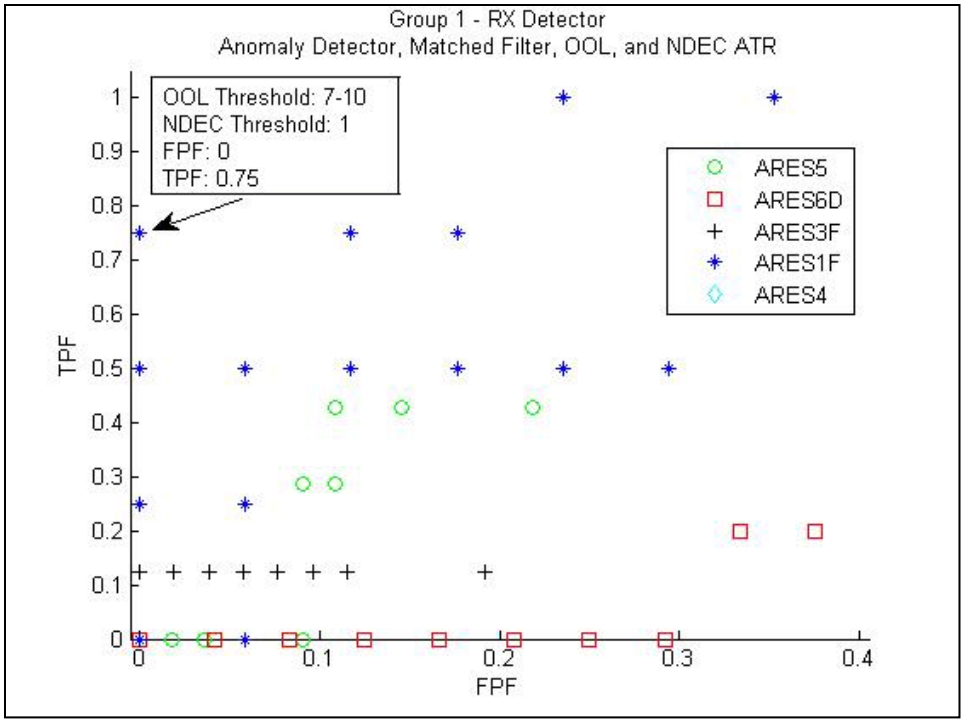

Figure 26. 4-Step ATR with RX detector TPF, FPF results for all OOL threshold and NDEC threshold combinations

Table 15. Recommended OOL and NDEC Threshold Levels for ATR with RX

ATR with RX	OOL Threshold Level	NDEC Threshold Level
4-Step	7, 8, 9, or 10	1
3-Step	7, 8, 9, or 10	n/a
2-Step	n/a	n/a

ATR with AutoGAD Anomaly Detector

TPF and FPF results for each combination of OOL threshold and NDEC threshold for the four-step ATR with the AutoGAD detector are provided in Figure 27. The ideal FPF is 0.167 and TPF is 0.167. This occurs at OOL threshold levels 3 - 5 and NDEC threshold level one. The OOL threshold was one for the three-step ATR. Obviously, there are no thresholds for the two-step ATR. A summary of the results are given in Table 16.

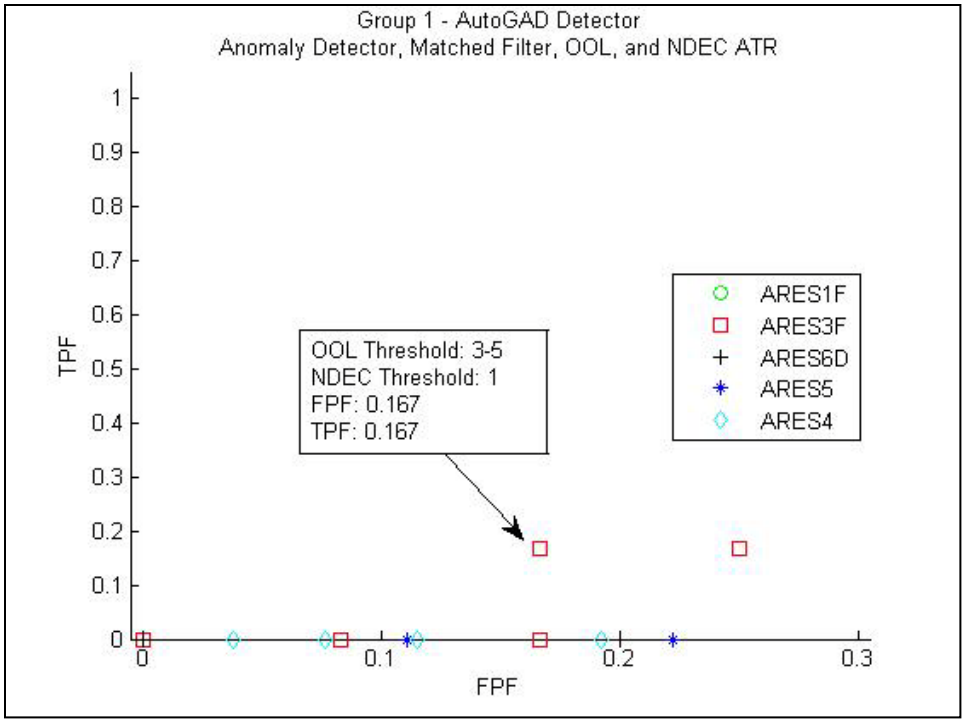

Figure 27. 4-Step ATR with AutoGAD detector TPF, FPF results for all OOL threshold and NDEC threshold combinations

Table 16. Recommended OOL and NDEC Threshold Levels for ATR with AutoGAD

ATR with AutoGAD	OOL Threshold Level	NDEC Threshold Level
4-Step	3, 4, or 5	1
3-Step	1	n/a
2-Step	n/a	n/a

Training Data Set Summary and Recommendations

Combining the results of the RX and AutoGAD four-step ATRs, Figure 28, it is obvious that the ATR with RX dominates the AutoGAD ATR. Therefore, the OOL threshold level that will be applied to the four-step ATR will nominally be eight and the NDEC threshold to be applied will be at level one. This domination by the RX ATR also occurred in the three-step

ATR, Figure 29. The three-step ATR will have an OOL threshold of eight, although any level seven through ten could have be chosen. The results are non-applicable for the two-step ATR.

The domination of RX results to AutoGAD results was an unexpected result. Examining the results indicate that although AutoGAD is a superior anomaly detector it is actually degrading the performance in the ATR process. This could be because AutoGAD is detecting more anomalies than RX; hence, it actually creates more opportunities to inaccurately label a detected anomaly.

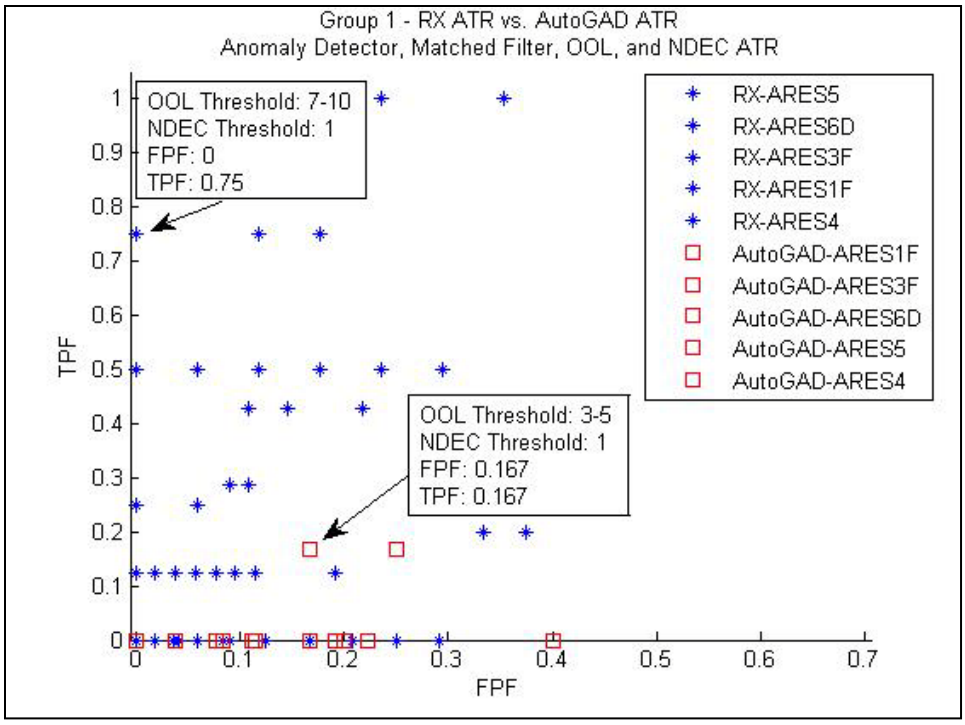

Figure 28. 4-Step RX ATR vs. AutoGAD ATR comparison of TPF, FPF results for all OOL threshold and NDEC threshold combinations

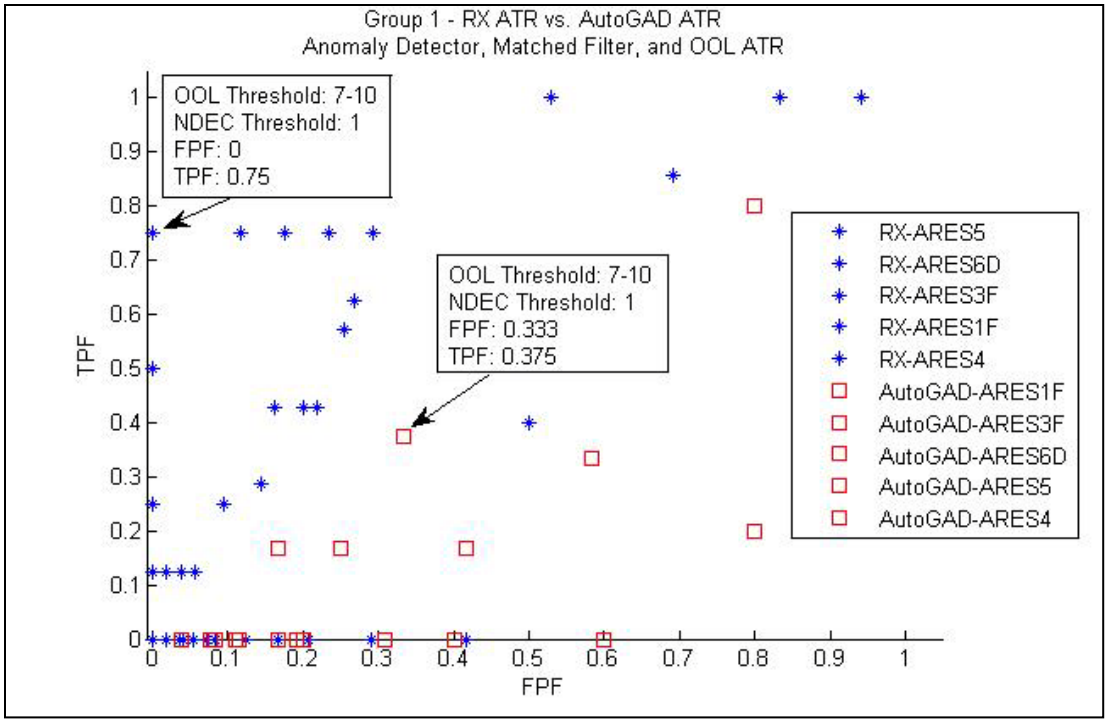

Figure 29. 3-Step RX ATR vs. AutoGAD ATR comparison of TPF, FPF results for all OOL threshold and NDEC threshold combinations

In regards to the two-step ATR with either ROI generator it was noticed the majority of TPF, FPF couples were (1,1). This is due to the fact that every anomaly was declared as one of the truth library objects at the end of the matched filter step and background labels were not given to anomalies until the OOL and/or NDEC decision steps. Therefore, a typical classification confusion matrix would resemble Table 17.

Table 17. Example Classification Confusion Matrix for 2-Step ATR

		Anomaly Identified as…	
		"Target"	"Background"
True Anomaly is…	Target	8	0
	Background	52	0

Test (Groups 2 and 3) Data Set Analysis

As a result of the previously mentioned domination by the RX ATR over the AutoGAD ATR, test data runs will only be for the RX ATR. They were completed in the following order, Table 18:

Table 18. Test Data Sets Run Order

Run Number	Image	Data Group Number	Run Number	Image	Data Group Number
1	ARES4F	3	5	ARES2D	3
2	ARES2F	3	6	ARES3D	2
3	ARES7F_10kFT	2	7	ARES1D	2
4	ARES5F	2			

Of the three performance measures for the seven images the most insight is gained with the classification FPF, columns 9 – 11 of Table 19. Recall for the two-step ATR the FPF was always 1. Comparing the three-step ATR to the full, we see that the FPF of the latter is always equal to or less than the prior. This is expected as detected anomalies can only be updated with background labels going from the three-step ATR to the other. For label accuracy and classification TPF it is difficult to note any trends. Where applicable the label accuracy increases from the two-step ATR to the three-step ATR but it decreases comparing three-step to the four-step ATR. A label accuracy of zero indicates no TP results occurred. The TPF performance measure also appears to decrease from three-step to four-step ATR. Zeros occur because of the detected anomalies only background labels are given, or FP labels. Not-a-number (NaN) results are given when no TP and FP results are available. Looking at Group 3 results they appear as expected with NaN labels for the TPF and low FPF scores.

Table 19. Testing Data Set Analysis Results plus four Training Data Set Images

Group	Image	Label Accuracy			Classification					
					TPF			FPF		
		4-Step	3-Step	2-Step	4-Step	3-Step	2-Step	4-Step	3-Step	2-Step
2	1D	0	0	0.070	0	0	1	0.042	0.042	1
2	3D	0.333	0.600	0.047	0.333	1	1	0.039	0.039	1
2	5F	NaN	0	0.017	0	0	1	0	0.017	1
2	7F	1	1	0.259	0.571	0.571	1	0	0	1
3	2D	0	0	0	NaN	NaN	NaN	0.057	0.057	1
3	2F	0	0	0	NaN	NaN	NaN	0.085	0.127	1
3	4F	0	0	0	NaN	NaN	NaN	0.057	0.057	1

Remember that the OOL threshold for the four-step ATR was chosen nominally to be eight when levels of seven, nine, and ten were also applicable. In an effort to assess if performance measures were affected by valid OOL threshold levels, level seven was also assessed. It was expected that by decreasing the threshold level label accuracy and TPF results in turn might increase. This assessment showed the opposite with an increase in FPF scores for three of the seven images, Table 20. These changes only occurred by adding one or two true background anomalies and labeling them as targets. Label accuracy and TPF measures did not change for all images. Levels nine and ten were not assessed because performance measures can only decrease. All classification confusion matrices and performance measures are located in Appendix C.

Table 20. OOL Threshold FPF Comparison

OOL Threshold	Group	Image	FPF		
			4-Step	3-Step	2-Step
7	2	1D	0.0588	0.0588	1
8	2	1D	0.0420	0.0420	1
7	3	2F	0.0986	0.1408	1
8	3	2F	0.0845	0.1268	1
7	2	5F	0.0169	0.0339	1
8	2	5F	0	0.0169	1

Recognition Evaluation

Overall, the performance in regards to recognition was low or non-existent. Across Group 2 images only one image, ARES7F_10kFT, recorded any TP counts for library targets for the four-step ATR process, Table 21. In Table 22, image ARES3D, there are FP counts for one target type in all three ATRs and for images ARES1D and ARES5F there were only FP or TP counts in the two-step ATR, Table 23 and Table 24 respectively.

Table 21. Image ARES7F_10kFT Recognition Confusion Matrix

4-Step ATR

	"M1"	"HMMWV"	"T-72"	"B"
M1	0	0	0	0
HMMWV	0	2	0	1
T-72	2	0	0	2
B	0	0	0	20

3-Step ATR

	"M1"	"HMMWV"	"T-72"	"B"
M1	0	0	0	0
HMMWV	0	2	0	1
T-72	2	0	0	2
B	0	0	0	20

2-Step ATR

	"M1"	"HMMWV"	"T-72"	"B"
M1	0	0	0	0
HMMWV	1	2	0	0
T-72	3	1	0	0
B	11	2	7	0

Table 22. Image ARES3D Recognition Confusion Matrix

4-Step ATR

	"M1"	"HMMWV"	"T-72"	"B"
M1	0	0	0	0
HMMWV	1	0	0	2
T-72	0	0	0	0
B	0	0	2	59

3-Step ATR

	"M1"	"HMMWV"	"T-72"	"B"
M1	0	0	0	0
HMMWV	3	0	0	0
T-72	0	0	0	0
B	0	0	2	59

2-Step ATR

	"M1"	"HMMWV"	"T-72"	"B"
M1	0	0	0	0
HMMWV	3	0	0	0
T-72	0	0	0	0
B	19	8	34	0

Table 23. Image ARES1D Recognition Confusion Matrix

4-Step ATR

	"M1"	"HMMWV"	"T-72"	"B"
M1	0	0	0	0
HMMWV	0	0	0	0
T-72	0	0	0	9
B	1	0	4	114

3-Step ATR

	"M1"	"HMMWV"	"T-72"	"B"
M1	0	0	0	0
HMMWV	0	0	0	0
T-72	0	0	0	9
B	1	0	4	114

2-Step ATR

	"M1"	"HMMWV"	"T-72"	"B"
M1	0	0	0	0
HMMWV	0	0	0	0
T-72	3	0	6	0
B	35	24	60	0

Table 24. Image ARES5F Recognition Confusion Matrix

4-Step ATR

	"M1"	"HMMWV"	"T-72"	"B"
M1	0	0	0	2
HMMWV	0	0	0	0
T-72	0	0	0	0
B	0	0	0	118

3-Step ATR

	"M1"	"HMMWV"	"T-72"	"B"
M1	0	0	0	2
HMMWV	0	0	0	0
T-72	0	0	0	0
B	2	0	0	116

2-Step ATR

	"M1"	"HMMWV"	"T-72"	"B"
M1	2	0	0	0
HMMWV	0	0	0	0
T-72	0	0	0	0
B	56	13	49	0

V. Discussion

Conclusions

The primary objective of this thesis was to develop a baseline, autonomous four-step ATR process for HSI. This was completed with the following steps: 1) ROI generator, 2) classification, 3) OOL decision, and 4) NDEC decision. During this study it was found that ATR performance was affected by the ROI generator. Specifically, when comparing TPF and FPF scores the ATR with the RX anomaly detector dominated the ATR using the AutoGAD anomaly detector.

Another objective, assessing the baseline four-step ATR process, demonstrated two points:

1) From a classification perspective, meaning the anomaly falls within the target library or it doesn't, the ATR process is feasible. From an operational perspective this could be useful added information if a decision maker were interested in locating a subset of targets.
2) From the recognition standpoint or the anomaly is correctly identified as a specific library target, the performance is low.

Finally, inclusion of the OOL and NDEC steps assisted in filtering detected anomalies from targets of interest to background anomalies or anomalies that are outside the scope of the target library.

Research Contributions

This thesis developed a baseline, autonomous four-step ATR process for HSI, while demonstrating that an ATR with a less adequate ROI generator was superior to an ATR with a more robust ROI generator in regards to TPF and FPF performance. Additionally, this research assessed how the incremental inclusion of the OOL step and NDEC step affect the performance of the ATR.

Further Research

Throughout this study new opportunities of investigation presented themselves as areas of future research. These opportunities include:

- Assess the vegetation index percentages to see if there is an ideal value for all images or perhaps image type as discussed in Chapter III.
- Utilize Robust Parameter Design techniques to determine optimal ATR settings. For example, using different techniques at each step.
- Further assess why a less adequate anomaly detector performs better as compared to the AutoGAD detector with regards to ATR performance.
- Look at the use of linear least-squares regression analysis for gain and offset estimates so that more than one known vegetation signature could be used for VN. Or study ATR performance with different vegetation signatures.
- Research using other image background means and covariance estimates for the classification step.

Appendix A: Vegetation Index Threshold Study: ROC Curves

ARES1D:

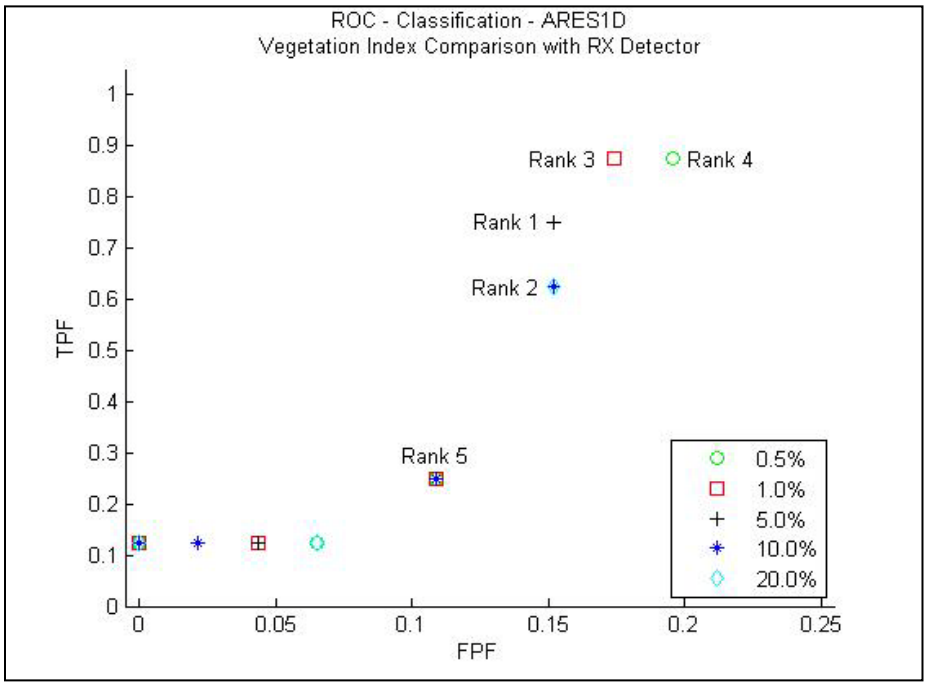

ARES1F:

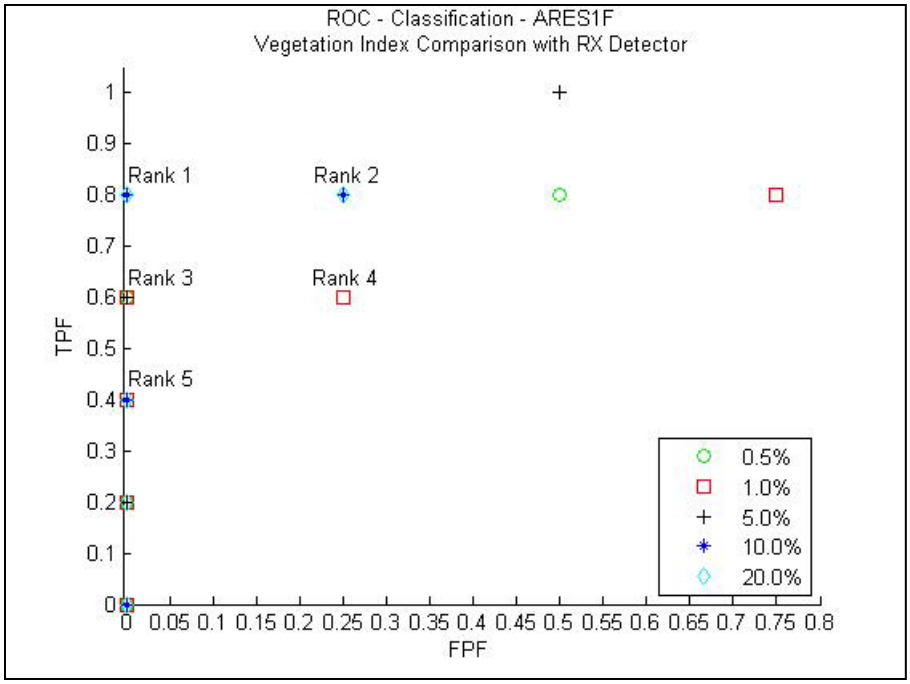

ARES3D:

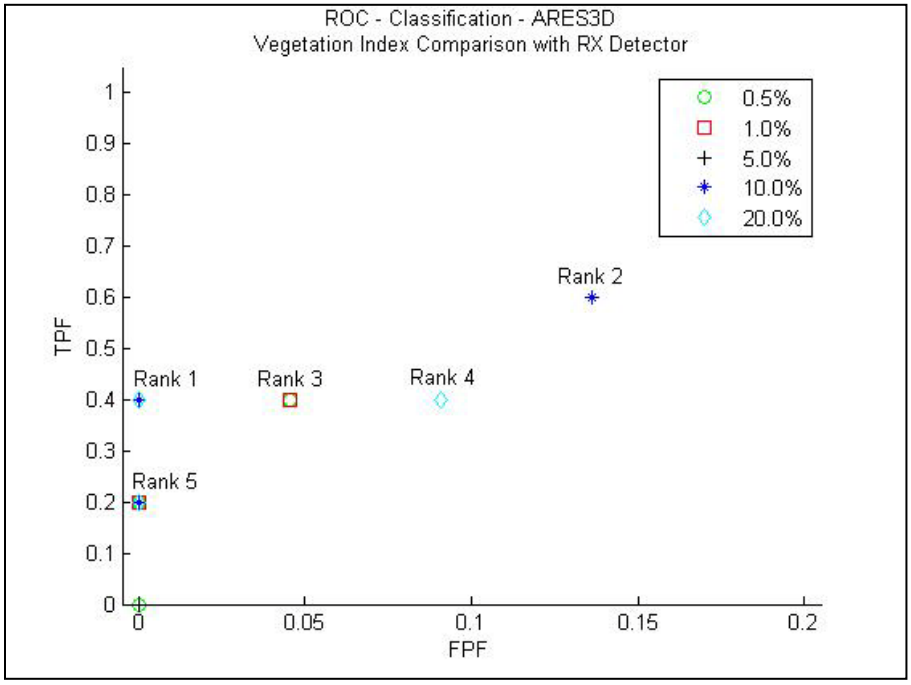

ARES3F:

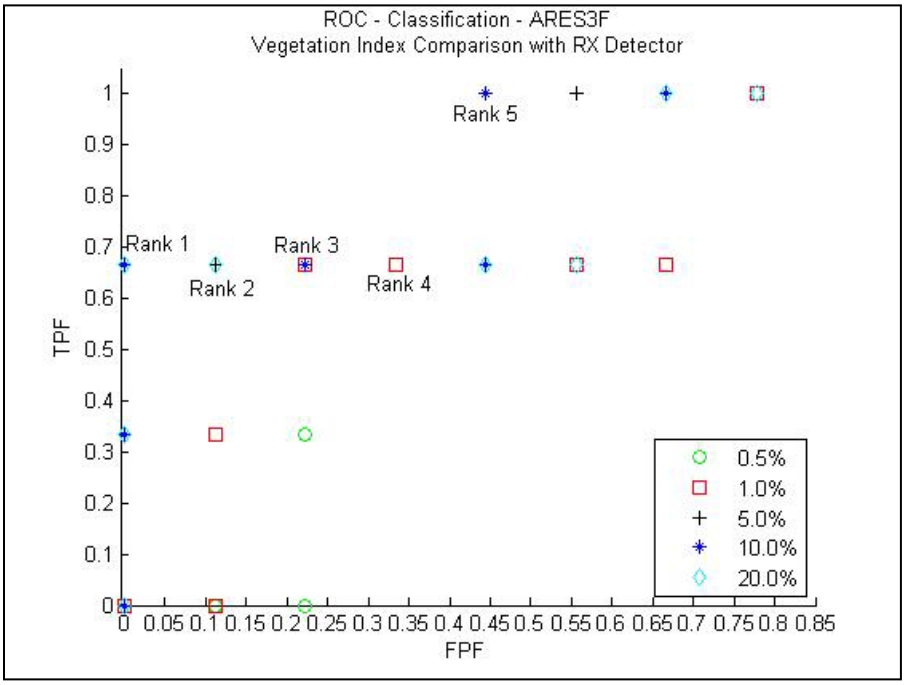

ARES5:

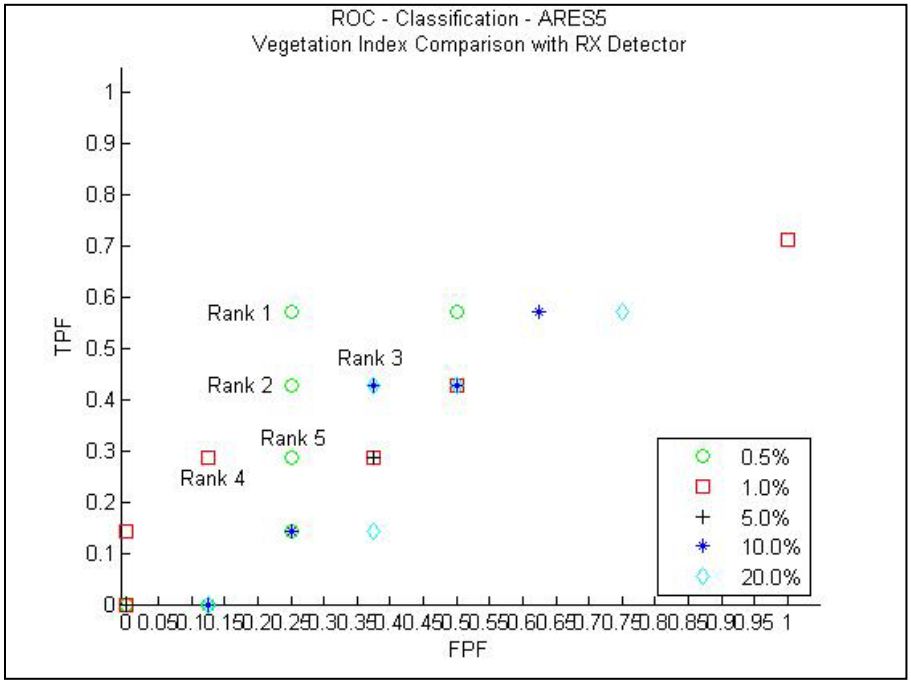

ARES6D_10kFT:

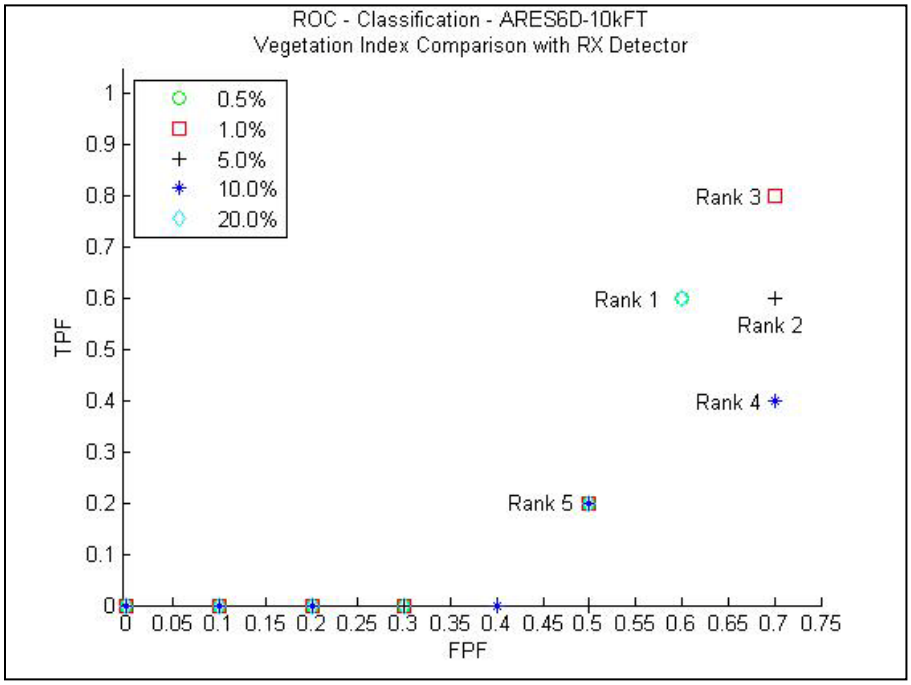

Appendix B: Vegetation Index Threshold Study: Ranking Comparison

ARES1D:

Ranking	Vegetation Index Percentage (%)				
	0.5	1.0	5.0	10.0	20.0
1			1		
2				2	2
3		3			
4	4				
5	5	5	5	5	
Sum	9	8	6	7	2
Average	4.5	4	3	3.5	2

ARES1F:

Ranking	Vegetation Index Percentage (%)				
	0.5	1.0	5.0	10.0	20.0
1				1	1
2				2	2
3	3	3	3		
4		4			
5		5	5	5	5
Sum	3	12	8	8	8
Average	3	4	4	2.667	2.667

ARES3D:

Ranking	Vegetation Index Percentage (%)				
	0.5	1.0	5.0	10.0	20.0
1				1	1
2			2	2	
3	3	3			
4					4
5	5	5	5	5	5
Sum	8	8	7	8	10
Average	4	4	3.5	2.667	3.333

ARES3F:

Ranking	Vegetation Index Percentage (%)				
	0.5	1.0	5.0	10.0	20.0
1			1	1	1
2			2		2
3		3	3	3	
4		4			
5			5	5	
Sum	n/a	7	11	9	3
Average	n/a	3.5	2.75	3	1.5

ARES5:

Ranking	Vegetation Index Percentage (%)				
	0.5	1.0	5.0	10.0	20.0
1	1				
2	2				
3			3	3	3
4		4			
5	5				
Sum	8	4	3	3	3
Average	2.667	4	3	3	3

ARES6D_10kFT:

Ranking	Vegetation Index Percentage (%)				
	0.5	1.0	5.0	10.0	20.0
1	1				1
2			2		
3		3			
4				4	
5	5	5		5	5
Sum	6	8	2	9	6
Average	3	4	2	4.5	3

Appendix C: Group 2 Performance Measure Tables

Test Images

ARES7F_10kFT: 4-Step ATR

Classification:

Label Accuracy	1
TPF	0.571429
FPF	0

Classification Confusion Matrix

	"Target"	"Background"
Target	4	3
Background	0	20

Recognition Confusion Matrix

	"M1"	"HMMWV"	"T-72"	"Background"
M1	0	0	0	0
HMMWV	0	2	0	1
T-72	2	0	0	2
Background	0	0	0	20

ARES7F_10kFT: 3-Step ATR

Classification:

Label Accuracy	1
TPF	0.571429
FPF	0

Classification Confusion Matrix

	"Target"	"Background"
Target	4	3
Background	0	20

Recognition Confusion Matrix

	"M1"	"HMMWV"	"T-72"	"Background"
M1	0	0	0	0
HMMWV	0	2	0	1
T-72	2	0	0	2
Background	0	0	0	20

ARES7F_10kFT: 2-Step ATR

Classification:

Label Accuracy	0.259259
TPF	1
FPF	1

Classification Confusion Matrix

	"Target"	"Background"
Target	7	0
Background	20	0

Recognition Confusion Matrix

	"M1"	"HMMWV"	"T-72"	"Background"
M1	0	0	0	0
HMMWV	1	2	0	0
T-72	3	1	0	0
Background	11	2	7	0

ARES3D: 4-Step ATR

Classification:

Label Accuracy	0.333333
TPF	0.333333
FPF	0.032787

Classification Confusion Matrix

	"Target"	"Background"
Target	1	2
Background	2	59

Recognition Confusion Matrix

	"M1"	"HMMWV"	"T-72"	"Background"
M1	0	0	0	0
HMMWV	1	0	0	2
T-72	0	0	0	0
Background	0	0	2	59

ARES3D: 3-Step ATR

Classification:

Label Accuracy	0.6
TPF	1
FPF	0.032787

Classification Confusion Matrix

	"Target"	"Background"
Target	3	0
Background	2	59

Recognition Confusion Matrix

	"M1"	"HMMWV"	"T-72"	"Background"
M1	0	0	0	0
HMMWV	3	0	0	0
T-72	0	0	0	0
Background	0	0	2	59

ARES3D: 2-Step ATR

Classification:

Label Accuracy	0.046875
TPF	1
FPF	1

Classification Confusion Matrix

	"Target"	"Background"
Target	3	0
Background	61	0

Recognition Confusion Matrix

	"M1"	"HMMWV"	"T-72"	"Background"
M1	0	0	0	0
HMMWV	3	0	0	0
T-72	0	0	0	0
Background	19	8	34	0

ARES1D: 4-Step ATR

Classification:

Label Accuracy	0
TPF	0
FPF	0.042017

Classification Confusion Matrix

	"Target"	"Background"
Target	0	9
Background	5	114

Recognition Confusion Matrix

	"M1"	"HMMWV"	"T-72"	"Background"
M1	0	0	0	0
HMMWV	0	0	0	0
T-72	0	0	0	9
Background	1	0	4	114

ARES1D: 3-Step ATR

Classification:

Label Accuracy	0
TPF	0
FPF	0.042017

Classification Confusion Matrix

	"Target"	"Background"
Target	0	9
Background	5	114

Recognition Confusion Matrix

	"M1"	"HMMWV"	"T-72"	"Background"
M1	0	0	0	0
HMMWV	0	0	0	0
T-72	0	0	0	9
Background	1	0	4	114

ARES1D: 2-Step ATR

Classification:

Label Accuracy	0.070313
TPF	1
FPF	1

Classification Confusion Matrix

	"Target"	"Background"
Target	9	0
Background	119	0

Recognition Confusion Matrix

	"M1"	"HMMWV"	"T-72"	"Background"
M1	0	0	0	0
HMMWV	0	0	0	0
T-72	3	0	6	0
Background	35	24	60	0

ARES5F: 4-Step ATR

Classification:

Label Accuracy	NaN
TPF	0
FPF	0

Classification Confusion Matrix

	"Target"	"Background"
Target	0	2
Background	0	118

Recognition Confusion Matrix

	"M1"	"HMMWV"	"T-72"	"Background"
M1	0	0	0	2
HMMWV	0	0	0	0
T-72	0	0	0	0
Background	0	0	0	118

ARES5F: 3-Step ATR

Classification:

Label Accuracy	0
TPF	0
FPF	0.016949

Classification Confusion Matrix

	"Target"	"Background"
Target	0	2
Background	2	116

Recognition Confusion Matrix

	"M1"	"HMMWV"	"T-72"	"Background"
M1	0	0	0	2
HMMWV	0	0	0	0
T-72	0	0	0	0
Background	2	0	0	116

ARES5F: 2-Step ATR

Classification:

Label Accuracy	0.016667
TPF	1
FPF	1

Classification Confusion Matrix

	"Target"	"Background"
Target	2	0
Background	118	0

Recognition Confusion Matrix

	"M1"	"HMMWV"	"T-72"	"Background"
M1	2	0	0	0
HMMWV	0	0	0	0
T-72	0	0	0	0
Background	56	13	49	0

Appendix D: Storyboard

Automatic Target Recognition for Hyperspectral Imagery

Capt Kelly Friesen
Advisor: Dr. Kenneth Bauer
Reader: Lt Col Mark Friend
Department of Operational Sciences (ENS)
Air Force Institute of Technology

Introduction

- Due to ever increasing data loads and decreasing DoD manning levels, more efficient algorithms are required to process data for the warfighter, specifically hyperspectral imagery (HSI)
- Anomaly Detection, Classification, Out-of-Library (OOL), and Non-Declaration (NDEC) are not new methods to HSI data processing
- Automatic Target Recognition (ATR) for HSI connects these four data processing methods into one automated process

Research Objectives

- Develop and assess baseline, autonomous four-step ATR process for HSI
- Assess performance differences between four-step ATR processes with different Region of Interest (ROI) generators
- Assess how incremental inclusion of OOL and NDEC steps affect ATR performance

AIR FORCE INSTITUTE OF TECHNOLOGY

ATR Methodology

Step 0: Import HSI data / remove atmospheric absorption bands

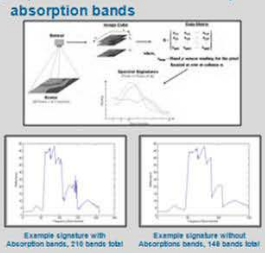

Example signature with Absorption bands, 210 bands total

Example signature without Absorptions bands, 148 bands total

Step 1a: ROI Generators

- Reed-Xiaoli (RX) Anomaly Detector Settings

$$RX(x) = (x-\hat{\mu})^T S^{-1}(x-\hat{\mu})$$

Preprocessing PCs	Alpha Level	Window Size
10 PCs retained	0.01	15x15 pixels

- Automatic Global Anomaly Detector (AutoGAD) Settings based on Johnson, 2008

Step 1b: Atmospheric Compensation

- Solve Linear Approximate:

$$\text{Rad}(\lambda) = \hat{a}(\lambda)\text{Refl}(\lambda) + \hat{b}(\lambda)$$

- where, Gain and Offset are respectively

$$\hat{a}(\lambda) = \frac{L_2(\lambda) - L_1(\lambda)}{\rho_2(\lambda) - \rho_1(\lambda)} \qquad \hat{b}(\lambda) = \frac{L_1(\lambda)\rho_2(\lambda) - L_2(\lambda)\rho_1(\lambda)}{\rho_2(\lambda) - \rho_1(\lambda)}$$

- Vegetation Normalization (VN) applied to estimate L_i and ρ_i
- Normalized-Difference Vegetation Index (NDVI)

$$NDVI = \frac{L_2(860nm) - L_2(660nm)}{L_2(860nm) + L_2(660nm)}$$

Step 2: Classification (Forced ID)

- Adaptive Matched Filter

$$AMF = \frac{\left[(z-\mu_b)^T \Sigma_b^{-1}(x-\mu_b)\right]^2}{(z-\mu_b)^T \Sigma_b^{-1}(z-\mu_b)}$$

Step 3: OOL Decision

- Threshold Technique:
  - Anomaly maximum average AMF score compared to threshold
  - Max. avg. AMF score ≥ Threshold
    => Anomaly labeled In-Library
    Max. avg. AMF score < Threshold
    => Anomaly labeled OOL

Step 4: NDEC Decision for final anomaly classification

- Threshold Technique:
  - Difference between top two max. avg. AMF scores compared to threshold
  - Difference ≥ Threshold
    => Anomaly Declared
  - Difference < Threshold
    => Anomaly labeled NDEC

Assessment Methodology

- Calculated True Positive Fraction (TPF) and False Positive Fraction (FPF) rates from Classification and Recognition perspectives
- Applied Receiver Operating Characteristic curve analysis

Contributions

- Developed baseline, autonomous four-step HSI ATR process
- Demonstrated ATR with less adequate ROI generator was superior to ATR with more robust ROI generator with respect to TPF and FPF performance
- Assessed how incremental inclusion of OOL step and NDEC step affect ATR performance

Future Research

- Find optimal vegetation index threshold percentage
- Utilize Robust Parameter Design techniques to determine optimal ATR settings, i.e., using different techniques at each step
- Further assess why ATR with less adequate ROI generator (RX) performs better then ATR with superior ROI generator (AutoGAD)
- Use linear least-squares regression analysis for gain and offset estimates to increase number of vegetation signatures used in VN or study ATR performance with different vegetation signatures
- Research add'l methods to estimate background mean and covariance

Bibliography

Albrecht, T. W. (2005). *Combat Identification with Sequential Observations, Rejection Option, and Out-of-Library Targets.* PhD Thesis AFIT-DS-ENS-05-03, Air Force Institute of Technology, WPAFB.

Alsing, S. G., Bauer, K. W., & Oxley, M. E. (2002). Convergence of Receiver Operatiing Characteristic Curves and the Performance of Neural Networks. *Smart Engineering System Design , Vol. 4* (2), 133-145.

Amit Banerjee, P. B., & Meth, R. (2007). Fast Hyperspectral Anomaly Detection Via SVDD. *IEEE* (1-4244-1437-7/07), IV-101 - IV-104.

Bannari, A., Asalhi, H., & Teillet, P. M. (2002). Transformed Difference Vegetation Index (TDVI) for Vegetation Cover Mapping. *IEEE* (0-7803-7536-X/02), 3053-3055.

Borghys, D., & Perneel, C. (2010). Study of the Influence of Pre-Processing of Local Statistics-Based Anomaly Detector Results. *IEEE* (978-1-4244-8907-7/10).

Bush, K. R. (2012). *Using QR Factorization for Real-Time Anomaly Detection in Hyperspectral Images.* Thesis AFIT-OR-MS-ENS-12-04, Air Force Institute of Technology, WPAFB.

Chang, C.-I., & Chiang, S.-S. (2002). Anomaly Detection and Classification for Hyperspectral Imagery. *IEEE Transactions on Geoscience and Remote Sensing , 40*, 1314-1325.

Chang, C.-I., & Chiang, S.-S. (2001). Real-time Processing Algorithms for Target Detection and Classification in Hyperspectral Imagery. *IEEE Transactions on Geoscience and Remote Sensing* , 39:760-768.

Chen, W., Liu, L., Zhang, C., Wang, J., Wang, J., & Pan, Y. (2004). Monitoring the Seasonal Bare Soil Areas in Beijun Using Mutil-Temporal TM Images. *Proceedings of the 2004 International Geoscience and Remote Sensing Symposium, Vol. 5*, pp. 3379-..82.

Chen, Y., Nasrabadi, N. M., & Tran, T. D. (2011). Sparse Representation for Target Detection in Hyperspectral Imagery. *IEEE Journal of Selected Topics in Signal Processing , Vol. 5* (no. 3), 629-640.

Chow, C. (1970). On Optimum Rejection Error and Reject Tradeoff. *IEEE Transactions on Information Theory , 16*, 41-46.

Connor, P. K., & Mooneyhan, D. W. (1985). *Practical Application of Landsat Data.* (A. Schnapf, Ed.) New York: AIAA.

Dillion, W. R., & Goldstein, M. (1984). *Multivariate Analysis: Methods and Application.* New York: John Wiley & Sons, Inc.

Du, P., Zhang, H., Yuan, L., Liu, P., & Zhang, H. (2007). Comparison of Vegetation Index from ASTER, CBERS and Landsat ETM+. *IEEE* (1-4244-1212-9/07), 3341-3344.

Eismann, M. T. (2011). Hyperspectral Remote Sensing. SPIE Press.

Eismann, M. T., Stocker, A. D., & Nasrabadi, N. M. (2009). Automated Hyperspectral Cueing for Civil Search and Rescue. *IEEE* (0018-9219), pgs. 1031-1055.

Fawcett, T. (2001). Using Rule Sets to Maximize ROC Performance. *IEEE International Conference on Data Mining, Vol. 8.*

Friend, M. A. (2007). *Combat Identification with Synthetic Aperture Radar, Out-of-Library Identification, and Non-Declarations.* PhD Thesis AFIT-DS-ENS-07-04, Air Force Institute of Technology, WPAFB.

Fumera, G., Roli, F., & Giacinto, G. (2000). Rejection Option with Multiple Thresholds. *Pattern Recognition , 33*, 2099-2101.

Gaucel, J.-M., Guillaume, M., & Bourennane, S. (2005). Whitening Spacial Correlation Filtering for Hyperspectral Anomaly Detection. *IEEE International Conference on Acoustics, Speech, and Signal Processing (ICASSP '05)* , 1:333-336.

Goldfein, D. L. (2012, January 4).

Healey, G., & Slater, D. (1999). Models and Methods for Automated Material Identification in Hyperspectral Imagery Acquired Under Unknown Illumination and Atmospheric Conditions. *IEEE Transactions on Geoscience and Remote Sensing* , 37:2706-2717.

Hsueh, M., & Chang, C.-I. (2004). Adaptive Causal Anomaly Detection for Hyperspectral Imagery. *IEEE Transactions on Geoscience and Remote Sensing (IGARSS '04)* , 5:3222-3224.

Huete, A. R. (1988). A soil-adjusted vegetation index (SAVI). *remoted Sensing of Environment , Vol. 25* (No. 3), 295-309.

Hyvärinen, A. (1999). Fast and Robust Fixed-Point Algorithms for Independent Component Analysis. *IEE Transactions on Neural Networks , Vol. 10* (No. 3), 626-634.

Ientilucci, E. J., & Bajorski, P. (2006). Statistical Models for Physically Derived Target Sub-spaces. *SPIE Porceedings on Imaging Spectrometry XI*, (p. 6302).

Johnson, R. J. (2008). *Improved feature extraction, feature selection, and identification techniques that create a fast unsupervised hyperspectral target detection algorithm.* Thesis, AFIT, Dept. of Operational Sciences.

Kerekes, J. P. (1998). Error Analysis of Spectral Reflectance from Imaging Spectrometer Data. *IEEE* (0-7803-4403-0/98), 2697-2701.

Kwon, H., & Nasrabadi, N. M. (2005). A Nonlinear Anomaly Detector for Hyperspectral Imagery. *IEEE Transactions on Geoscience and Remote Sensing* , 43:388-397.

Laine, T. I. (2005). *Optimization of Automatic Target Recognition with a Reject Option Using Fusion and Correlated Sensor Data.* Ph.D. thesis, Air Force Institute of Technology, Wright-Patterson AFB OH.

Landgrebe, D. A. (2003). *Signal Theory Methods in Multispectral Remote Sensing.* Hoboken, New Jersey: John Wiley & Sons, Inc.

Leap, N. J. (2008). *A Confidence Paradigm for Classification Systems.* PhD Thesis AFIT-DS-ENS-08-02, Air Force Institute of Technology, WPAFB.

Lillisand, T. M., & Kiefer, R. W. (2000). *Remote sensing and image interpretation.* New York, New York: John Wiley and Sons Inc.

Madar, E., Kuybeda, O., Malah, D., & Barzohar, M. (2009). Local-Global Background Modeling for Anomaly Detection in Hyperspectral Images. *IEEE* (978-1-4244-4687-2/09).

Manolakis, D., & Shaw, G. (2002, January). Detection Algorithms for Hyperspectral Imaging Applications. *IEEE Signal Processing Magazine* , 29-43.

Manolakis, D., Lockwood, R., Cooley, T., & Jacobson, J. (2009). Is There a Best Hyperspectral Detection Algorithm. *Proceedings SPIE Algorithms and Technologies for Multispectral, Hyperspectral, and Ultraspectral Imagery XV, Vol. 7334*, pp. 1-16.

Manolaksi, D., Zhang, D., Rossacci, M., Lockwood, R., Cooley, T., & Jacobson, J. Maintaining CFAR Operation in Hyperspectral Target Detection Using Extreme Value Distributions. *Proceedings of SPIE , Vol. 6565*.

Merriam-Webster. (n.d.). Retrieved January 16, 2012, from Merriam-Webster Web site: http://www.merriam-webster.com/dictionary/detection

Paul, A. S., & Shaw, A. K. *Robust HRR Radar Target Identification by Hybridization of HMM and Eigen-Template based Matched Filtering.* Wright State University, Electrical Engineering Department, Dayton, OH.

Paul, A. S., Shaw, A. K., Das, K., & Mitra, A. K. (2003). Improved HRR-ATR using Hybridization of HMM and Eigen-Template-Matched Filtering. *IEEE* , 397-400.

Qinjiu, T., & Xiangjun, M. (1998). Advances in study on vegetation indices. *Advance in earth science , Vol. 13* (No. 4), 327-333.

Ratner, B. (n.d.). *Overfitting: Old Problem, New Solution*. Retrieved Nov. 4, 2011, from GenIQ Model: http://geniq.net/overfitting-old-problem-new-solution.html

Reed, I. S., & Yu, X. (1990). Adaptive Multiple-Band CFAR Detection of an Optical Pattern with Unknown Spectral Distribution. *IEEE Transactions on Acoustics, Speech, and Signal Processing , Vol. 38* (No. 10), 1760-1770.

Richards, J., & Bray, B. K. *An informative confidence metric in ATR.*

Rickard, L. J., Basedow, R., Zalewski, E., & Silverglate, P. (1993). HYDICE: An airborne system for hyperspectral imaging. *Proceedings of the SPIE , Vol. 1937*, 173-179.

Riley, R., Newsome, R. K., & Andrews, A. K. (2004). Anomaly Detection in Noisy Hyperspectral Imagery. *SPIE Conference on Imaging Spectrometry X* , 5546:159-170.

Robey, F. C., Fuhrmann, D. R., Kelly, E. J., & Nitzburg, R. (1992). A CFAR adaptive matched filter detector. *IEEE Transactions onAerospace and Electronic Systems , Vol. 28* (no. 1), 208-216.

Robila, S. A., & Varshney, P. K. (2022). Target Detection in Hyperspectral Images Based on Independent Component Analysis. *Proceedings of SPIE Automatic Target Recognition XII, Vol. 4729*, pp. 173-183.

Rosario, D. (2006). *Alternative Asymmetric Hypothesis Tests for Hyperspectral Imagery.* Army Research Laboratory, Sensors and Electron Devices Directorate, Adelphi, MD 20783-1145.

Ross, T., & Minardi, M. (2004). Discrimination and Confidence Error in Detector Reported Scores. *Proceedings of SPIE: Algorithms for Synthetic Aperature Radar Imagery XI, Vol. 5427.*

Rouse, J. W., Hass, R. H., Schell, J. A., & Deering, D. W. (1973). Monitoring Vegetation Systems in the Great Plains with ERTS. *In Proceeding of the Third ERTS Symposium, Vol. 1*, pp. 309-317.

Schaum, A. P. (2006). A Remedy for Nonstationarity in Background Transition Regions for Real Time Hyperspectral Detection. *Proceedings of the 2006 IEEE Aerospace Conference.*

Schaum, A. P. (2004). Joint Subspace Detection of Hyperspectral Targets. *Proceedings of the 2004 IEEE Aerospace Conference*, (pp. 3:1818-1824).

Shaw, G., & Manolakis, D. (2002). Signal Processing for Hyperspectral Image Exploitation. *IEEE Signal Processing Magazine , Vol. 19* (no.1), 12-16.

Smetek, T. E. (2007). *Hyperspectral Imagery Target Detection Using Improved Anomaly Detection and Signature Matching.* PhD Thesis AFIT-DS-ENS-07-07, Air Force Institute of Technology, WPAFB.

Smetek, T. E., & Bauer, K. W. (2008). A Comparison of Multivariate Outlier Detection Methods for Finding Hyperspectral Anomalies. *Military Operations Research , V13 N4*, 19-43.

SpecTIR: Imagery with Substance. (n.d.). Retrieved October 2011, from http://www.spectir.com/ref.htm

Stein, D. W., Beaven, S. G., Hoff, L. E., Winter, E. M., Schaum, A. P., & Stocker, A. D. (2002, January). Anomaly Detection from Hyperspectral Imagery. *IEEE Signal Processing Magazine* , 58-69.

Taitano, Y. P., Geier, B. A., & Bauer, K. W. (2010). A Locally Adaptable Iterative RX Detector. *EURASIP J. Adv. Signal Process., Special Issue on Adv. Image Process. for Defense and Security Applicat. , vol. 2010*.

Turnbaugh, M. A. (2009). *A Hybrid Template-Based Composite Classification System.* PhD Thesis AFIT-DS-ENS-08-04, Air Force Institute of Technology, WPAFB.

Turnquist, B. R. (2011). *Fusion Schemes for Ensembles of Hyperspectral Anomaly Detection Algorithms.* Thesis AFIT-OR-MS-ENS-11-25, Air Force Institute of Technology, WPAFB.

West, J. E., Messinger, D. W., Ientilucci, E. J., Kerekes, J. P., & Schott, J. R. (2005). Matched Filter Stochastic Background Characterization for Hyperspectral Target Detection. *SPIE Conference on Algorithms and Technologies for Multispectral, Hyperspectral, and Ultraspectral Imagery XI*, (pp. 5806:1-12).

Williams, J. P., Bihl, T. J., & Bauer, K. W. (n.d.). Towards the Mitigation of Correlation Effects in Anomaly Detection for Hyperspectral Imagery. *Manuscript Submitted for Publication* .

VITA

Captain Kelly D. Friesen graduated from Hutchinson High School in Hutchinson, Kansas. He then graduated from Hutchinson Community College in Hutchinson, Kansas and Bethany College in Lindsborg, Kansas culminating in a Bachelor of Arts degree in Mathematics in May 2001. After graduation he worked at IBT in Hutchinson until he attended the United States Air Force Officer Training School in May 2003. On August 8, 2003 he was commissioned a second lieutenant.

His first assignment was at Kirtland AFB, NM as a weapon system analyst completing a variety of studies for the Office of Aerospace Studies. In October 2006, he was assigned to the B-2 Test Team at Whiteman AFB, MO where he was responsible for various aspects of Operational Test and Evaluation of the B-2. Then in August 2010, he entered the Graduate School of Engineering and Management, Air Force Institute of Technology to pursue a Master of Science degree in Operations Research. Upon graduation in March 2012, he will be assigned to the Head Quarters Air Force Recruiting Service at Randolph AFB, TX.

REPORT DOCUMENTATION PAGE

Form Approved
OMB No. 074-0188

1. REPORT DATE *(DD-MM-YYYY)*	2. REPORT TYPE	3. DATES COVERED *(From – To)*
22-03-2012	**Master's Thesis**	Jun 2011 – Mar 2012

4. TITLE AND SUBTITLE

Automatic Target Recognition for Hyperspectral Imagery

5a. CONTRACT NUMBER

5b. GRANT NUMBER

5c. PROGRAM ELEMENT NUMBER

6. AUTHOR(S)

Friesen, Kelly D., Captain, USAF

5d. PROJECT NUMBER

5e. TASK NUMBER

5f. WORK UNIT NUMBER

7. PERFORMING ORGANIZATION NAMES(S) AND ADDRESS(S)
Air Force Institute of Technology
Graduate School of Engineering and Management (AFIT/EN)
2950 Hobson Street, Building 642
WPAFB OH 45433-7765

8. PERFORMING ORGANIZATION REPORT NUMBER

AFIT-OR-MS-ENS-12-11

9. SPONSORING/MONITORING AGENCY NAME(S) AND ADDRESS(ES)
NASIC/DAIR
ATTN: Mr. John Jacobson
4180 Watson Way
WPAFB OH 45433-5648

10. SPONSOR/MONITOR'S ACRONYM(S)

11. SPONSOR/MONITOR'S REPORT NUMBER(S)

12. DISTRIBUTION/AVAILABILITY STATEMENT
DISTRIBUTION STATEMENT A: APPROVED FOR PUBLIC RELEASE; DISTRIBUTION UNLIMITED.

13. SUPPLEMENTARY NOTES

14. ABSTRACT
Automatic target detection and recognition in hyperspectral imagery offer passive means to detect and identify anomalies based on their material composition. In many combat identification approaches through pattern recognition, a minimum level of confidence is expected with costs associated with labeling anomalies as targets, non-targets or out-of-library. This research approaches the problem by developing a baseline, autonomous four step automatic target recognition (ATR) process: 1) anomaly detection, 2) spectral matching, 3) out-of-library decision, and 4) non-declaration decision. Atmospheric compensation techniques are employed in the initial steps to compare truth library signatures and sensor processed signatures. ATR performance is assessed and additionally contrasted to two modified ATRs to study the effects of including steps three and four. Also explored is the impact on the ATR with two different anomaly detection methods.

15. SUBJECT TERMS
hyperspectral imagery, automatic target recognition, anomaly detection, classification, out-of-library, non-declaration

16. SECURITY CLASSIFICATION OF:			17. LIMITATION OF ABSTRACT	18. NUMBER OF PAGES	19a. NAME OF RESPONSIBLE PERSON
a. REPORT	b. ABSTRACT	c. THIS PAGE			Dr. Kenneth W. Bauer (ENS)
U	U	U	UU	88	19b. TELEPHONE NUMBER *(Include area code)* (937) 255-3636, ext 4631; e-mail: Kenneth.Bauer@afit.edu

Standard Form 298 (Rev. 8-98)
Prescribed by ANSI Std. Z39-18